

An entropy stable spectral vanishing viscosity for discontinuous Galerkin schemes: application to shock capturing and LES models

Andrés Mateo-Gabín · Juan Manzanero · Eusebio Valero

Received: date / Accepted: date

Abstract We present a stable spectral vanishing viscosity for discontinuous Galerkin schemes, with applications to turbulent and supersonic flows. The idea behind the SVV is to spatially filter the dissipative fluxes, such that it concentrates in higher wavenumbers, where the flow is typically under-resolved, leaving low wavenumbers dissipation-free. Moreover, we derive a stable approximation of the Guermond–Popov fluxes with the Bassi–Rebay 1 scheme, used to introduce density regularization in shock capturing simulations. This filtering uses a Cholesky decomposition of the fluxes that ensures the entropy stability of the scheme, which also includes a stable approximation of boundary conditions for adiabatic walls. For turbulent flows, we test the method with the three-dimensional Taylor–Green vortex and show that energy is correctly dissipated, and the scheme is stable when a kinetic energy preserving split-form is used in combination with a low dissipation Riemann solver. Finally, we test the shock capturing capabilities of our method with the Shu–Osher and the supersonic forward facing step cases, obtaining good results without spurious oscillations even with coarse meshes.

Keywords discontinuous Galerkin · entropy stability · kinetic energy preserving · Large Eddy Simulation · shock capturing · spectral vanishing viscosity

1 Introduction

The central role that differential equations play in science and engineering explain the great interest and the efforts made to develop ever more efficient and accurate methods. In the field of fluid mechanics, high-order discontinuous Galerkin methods [1, 2] seem to lay in a sweet spot, being suitable

Andrés Mateo Gabín (E-mail: andres.mgabin@upm.es) · Juan Manzanero · Eusebio Valero
ETSIAE-UPM - School of Aeronautics, Universidad Politécnica de Madrid. Plaza Cardenal Cisneros 3, 28040 Madrid, Spain

Andrés Mateo-Gabín · Juan Manzanero · Eusebio Valero
Center for Computational Simulation, Universidad Politécnica de Madrid, Campus de Montegancedo, Boadilla del Monte, 28660, Madrid, Spain.

for complex geometries and easily allowing the introduction of h/p mesh adaptation to spectrally increase the accuracy [3, 4, 5, 6]. Nevertheless, the numerical dissipation they can introduce is limited and, even with the addition of inter-element numerical fluxes [7], it is not sufficient for challenging cases such as supersonic flows, where the Navier–Stokes equations allow discontinuous solutions that need higher rates of dissipation when approximated by high-order polynomials. In this situation it is desirable that the solver is able to maintain an ever decreasing entropy, according to the second law of thermodynamics.

The mathematical entropy is a well established framework to represent conservation laws. This mathematical entropy is arbitrarily defined such that is ever decreasing [8, 9, 10]. Hence, in kinetic-energy preserving schemes, the mathematical entropy is the kinetic energy, whereas in thermodynamic entropy preserving schemes, it is minus the thermodynamic entropy (which is ever increasing). In the case of the Discontinuous Galerkin Spectral Element Method (DGSEM) [11] with Gauss–Lobatto (GL) points, the polynomial derivative operator satisfies the discrete Summation–By–Parts Simultaneous–Approximation–Term (SBP–SAT) property [12, 13], which has led the development of split-form schemes that preserve the discrete entropy [14]. However, in the context of supersonic flows and shock capturing, where the flow variables can experience large oscillations, the use of an entropy preserving method does not guarantee its stability. This is because the entropy stability condition rests on a positive density, which is usually not the case as a result of the violent density oscillations at the vicinity of shocks. One way to alleviate this problem is the use of shock capturing methods that introduce some sort of density regularization, while keeping discrete entropy preservation. This point is a focus of active research and the literature contains several strategies that can be divided in two main branches. The first group makes use of the discretization to introduce the required additional dissipation. By lowering the order of the approximation, the dissipation of the numerical fluxes is introduced at lower wavenumbers, reducing the slope of the wave and smoothing the solution [15]. The other approach consists in adding dissipation directly in the driving equations, usually through a second order elliptic term [16, 17]. Nevertheless, the discontinuity limits the attainable accuracy and elements containing them can never reach spectral convergence [18]. In this work we focus on the second method and we derive two different approaches; first, a thermodynamic entropy stable scheme that uses a spectral vanishing viscosity (SVV) based on the fluxes proposed by Guermond and Popov [19], and second, a kinetic energy preserving scheme with its fluxes based on the physical Navier–Stokes viscosity. The use of the SVV makes it possible to modulate the dissipation in the wavenumber domain, and allows us to continuously shift from a low (second order) to a high-order dissipation.

Moreover, the SVV approach is also suitable for under-resolved turbulent flows, where the mesh cannot capture all the scales involved and the high-order DGSEM might not dissipate the correct amount of energy [20, 21, 22]. Several strategies have also been proposed for these types of flows, being the Reynolds Averaged Navier–Stokes (RANS) equations [23] and Large Eddy Simulations (LES) among the most extended. Implicit LES (iLES) methods benefit from the scheme’s numerical dissipation [24], while explicit LES methods model the effect of the small scales that cannot be accurately resolved into additional dissipation. In this work, we follow [25, 26] and couple the SVV and LES approaches so that the intensity is computed with the LES–Smagorinsky model, and it is then filtered by the SVV. However, we modify the SVV discretization such that the resulting scheme is kinetic energy preserving.

The structure of the rest of the paper is as follows: we briefly describe the compressible Navier–Stokes equations in Sec. 2, where we also highlight the entropy variables and introduce the artificial viscosity fluxes that will be used later. We then show the foundation of the DGSEM in Sec. 3 and, in Sec. 4, we detail the novel filtering technique that we use in the SVV formulation. Sec. 5.1 contains a detailed analysis of the stability of the entropy formulation with artificial viscosity, and in Sec. 5.2 we perform von Neumann analyses of the SVV applied to a one–dimensional advection–diffusion equation to preview its dissipation properties. Finally, Sec. 6 shows some numerical results with test cases in one to three dimensions: the Shu–Osher shock tube, a supersonic forward facing step and the inviscid Taylor–Green vortex.

1.1 Notation

The mathematical formulation of partial differential equations introduces the concepts of space vectors in \mathbb{R}^3 like $\vec{x} = (x, y, z)^T$, and state vectors in \mathbb{R}^5 , such as $\mathbf{q} = (\rho, \rho u, \rho v, \rho w, \rho e)^T$, to gather the field variables. We adopt the notation in [27], where a block vector represents an entity contained in the space $\mathbb{R}^3 \times \mathbb{R}^5$, e.g., fluxes, as three state vectors stacked on top of each other,

$$\overset{\leftrightarrow}{\mathbf{f}} = \begin{pmatrix} \mathbf{f}_1 \\ \mathbf{f}_2 \\ \mathbf{f}_3 \end{pmatrix} = \begin{pmatrix} \mathbf{f} \\ \mathbf{g} \\ \mathbf{h} \end{pmatrix}. \quad (1)$$

We can now extend the usual multiplication operators of calculus to vectors of different nature by acting on each subspace separately,

$$\overset{\leftrightarrow}{\mathbf{f}} \cdot \overset{\leftrightarrow}{\mathbf{g}} = \sum_{i=1}^3 \mathbf{f}_i^T \mathbf{g}_i, \quad \vec{g} \cdot \overset{\leftrightarrow}{\mathbf{f}} = \sum_{i=1}^3 g_i \mathbf{f}_i, \quad \vec{g} \mathbf{f} = \begin{pmatrix} g_1 \mathbf{f} \\ g_2 \mathbf{f} \\ g_3 \mathbf{f} \end{pmatrix}, \quad (2)$$

and, by setting $\vec{g} = \vec{\nabla}$, we obtain the expressions for the divergence and gradient operators,

$$\vec{\nabla} \cdot \overset{\leftrightarrow}{\mathbf{f}} = \sum_{i=1}^3 \frac{\partial \mathbf{f}_i}{\partial x_i}, \quad \vec{\nabla} \mathbf{q} = \begin{pmatrix} \mathbf{q}_x \\ \mathbf{q}_y \\ \mathbf{q}_z \end{pmatrix}. \quad (3)$$

Likewise, we define state matrices, \underline{A} , of size 5×5 to operate on the field variables, and block matrices as a combination of state matrices,

$$\mathcal{A} = \begin{pmatrix} \underline{A}_{11} & \underline{A}_{12} & \underline{A}_{13} \\ \underline{A}_{21} & \underline{A}_{22} & \underline{A}_{23} \\ \underline{A}_{31} & \underline{A}_{32} & \underline{A}_{33} \end{pmatrix}. \quad (4)$$

and thus, the product of matrices and vectors of the same type is well defined. We can also construct block versions of space matrices as follows. For example, consider the product

$$\vec{g} = \mathbf{M} \vec{f}. \quad (5)$$

that involves a space matrix $M \in \mathbb{R}^{3 \times 3}$. Its associated block matrix $\mathcal{M} \in \mathbb{R}^{15 \times 15}$ is created so that it is equivalent to apply (5) to each of the variables of the state components of the block vector, $\overset{\leftrightarrow}{\mathbf{f}}$,

$$\overset{\leftrightarrow}{\mathbf{g}} = \mathcal{M} \overset{\leftrightarrow}{\mathbf{f}}, \quad \mathcal{M} = \begin{pmatrix} M_{11} \underline{I}_5 & M_{12} \underline{I}_5 & M_{13} \underline{I}_5 \\ M_{21} \underline{I}_5 & M_{22} \underline{I}_5 & M_{23} \underline{I}_5 \\ M_{31} \underline{I}_5 & M_{32} \underline{I}_5 & M_{33} \underline{I}_5 \end{pmatrix}, \quad (6)$$

For more details, see [27]. We finally represent integrals in the domain Ω in bracket notation, $\langle \cdot \rangle$, being $\langle \cdot, \cdot \rangle$ the inner product in the same region,

$$\langle f \rangle = \int_{\Omega} f \, d\vec{x}, \quad \langle f, g \rangle = \int_{\Omega} fg \, d\vec{x}. \quad (7)$$

2 The compressible Navier–Stokes equations with artificial viscosity

In this section we describe the compressible Navier–Stokes equations. For the purpose of this work, we will complement the set of equations with additional dissipative terms, of which we consider two: locally increasing the molecular viscosity (Boussinesq’s approximation), and the entropy stable dissipative flux derived by Guermond and Popov in [19]. These fluxes are detailed in Sec. 2.2. Finally, in Sec. 2.3 we study the kinetic energy and entropy stability of the schemes derived.

The compressible Navier–Stokes equations with artificial viscosity are a set of non–linear advection–diffusion equations,

$$\mathbf{q}_t + \vec{\nabla} \cdot \overset{\leftrightarrow}{\mathbf{f}}_e = \vec{\nabla} \cdot \overset{\leftrightarrow}{\mathbf{f}}_v + \vec{\nabla} \cdot \overset{\leftrightarrow}{\mathbf{f}}_a. \quad (8)$$

The state vector is $\mathbf{q} = (\rho, \rho \vec{u}, \rho e)^T$ where ρ is the density, $\vec{u} = (u, v, w)^T$ is the velocity, and ρe is the total energy,

$$\rho e = \rho e_i + \frac{1}{2} \rho |\vec{u}|^2, \quad e_i = \frac{p/\rho}{\gamma - 1}, \quad p = \rho R T, \quad (9)$$

being e_i the internal energy, p the pressure, T the temperature, R the ideal gas constant, and γ the specific heat ratio. The inviscid fluxes $\overset{\leftrightarrow}{\mathbf{f}}_e$ depend on the state vector,

$$\mathbf{f}_e = \begin{pmatrix} \rho u \\ \rho u^2 + p \\ \rho uv \\ \rho uw \\ \rho hu \end{pmatrix}, \quad \mathbf{g}_e = \begin{pmatrix} \rho v \\ \rho v^2 + p \\ \rho vw \\ \rho hv \end{pmatrix}, \quad \mathbf{h}_e = \begin{pmatrix} \rho w \\ \rho uw \\ \rho vw \\ \rho w^2 + p \\ \rho hw \end{pmatrix}, \quad (10)$$

where $h = e + p/\rho$ is the total enthalpy. The viscous fluxes $\overset{\leftrightarrow}{\mathbf{f}}_v$ are

$$\mathbf{f}_v = \begin{pmatrix} 0 \\ \tau_{11} \\ \tau_{21} \\ \tau_{31} \\ \vec{\tau}_1 \cdot \vec{u} + q_1 \end{pmatrix}, \quad \mathbf{g}_v = \begin{pmatrix} 0 \\ \tau_{12} \\ \tau_{22} \\ \tau_{32} \\ \vec{\tau}_2 \cdot \vec{u} + q_2 \end{pmatrix}, \quad \mathbf{h}_v = \begin{pmatrix} 0 \\ \tau_{13} \\ \tau_{23} \\ \tau_{33} \\ \vec{\tau}_3 \cdot \vec{u} + q_3 \end{pmatrix}, \quad (11)$$

with $\tau_{ij} = \mu \left(\partial u_i / \partial x_j + \partial u_j / \partial x_i - \frac{2}{3} \vec{\nabla} \cdot \vec{u} \delta_{ij} \right)$ the stress tensor, $\vec{\tau}_i = (\tau_{1i}, \tau_{2i}, \tau_{3i})$ the stress in the three spatial directions, and \vec{q} the heat flux,

$$\vec{q} = \kappa \vec{\nabla} T. \quad (12)$$

The coefficients μ and κ are the molecular viscosity and thermal conductivity, related through the Prandtl number,

$$\kappa = \theta \mu R, \quad \theta = \frac{\gamma}{(\gamma - 1) \text{Pr}} \quad (13)$$

Finally, two different approaches to include additional dissipation are considered:

1. Increasing the molecular viscosity, μ_a , $\overset{\leftrightarrow}{\mathbf{f}}_a = \overset{\leftrightarrow}{\mathbf{f}}_v(\mu_a)$,
2. The Guermond–Popov flux, $\overset{\leftrightarrow}{\mathbf{f}}_a = \overset{\leftrightarrow}{\mathbf{f}}_{\text{GP}}(\mu_a, \alpha_a)$, developed in [19] that introduces two additional viscosity parameters, α_a and μ_a , which will be explained in more detail in Sec. 2.2.3,

$$\overset{\leftrightarrow}{\mathbf{f}}_{\text{GP}} = \alpha_a \begin{pmatrix} \vec{\nabla} \rho \\ \vec{\nabla} \rho \otimes \vec{u} \\ \vec{\nabla} (\rho e_i) + \frac{1}{2} |\vec{u}|^2 \vec{\nabla} \rho \end{pmatrix} + \mu_a \begin{pmatrix} 0 \\ \rho \vec{\nabla}^s \vec{u} \\ \rho \vec{u} \cdot \vec{\nabla}^s \vec{u} \end{pmatrix}, \quad \vec{\nabla}^s \vec{u} = \frac{1}{2} (\vec{\nabla} \vec{u} + \vec{\nabla} \vec{u}^T). \quad (14)$$

2.1 Entropy pairs and entropy variables

Now, in order to further analyze the entropy stability properties of our formulation in later sections, we introduce the concept of mathematical entropy. Starting from a generic conservation law in three dimensions,

$$\mathbf{q}_t + \vec{\nabla} \cdot \overset{\leftrightarrow}{\mathbf{f}} = 0, \quad (15)$$

we define the entropy [8, 9, 10, 28], \mathcal{E} , as a convex function on the variables \mathbf{q} that also satisfies

$$(\mathcal{E}_{\mathbf{q}})^T \overset{\leftrightarrow}{\mathbf{f}}_{\mathbf{q}} = \vec{f}_{\mathbf{q}}^{\mathcal{E}}, \quad \overset{\leftrightarrow}{\mathbf{f}}_{\mathbf{q}} = (\mathbf{f}_{\mathbf{q}}, \mathbf{g}_{\mathbf{q}}, \mathbf{h}_{\mathbf{q}})^T, \quad (16)$$

for the entropy–entropy flux pair $(\mathcal{E}, \vec{f}_{\mathbf{q}}^{\mathcal{E}})$. The derivative of \mathcal{E} is given the name of entropy variables,

$$\mathbf{w} = \mathcal{E}_{\mathbf{q}}, \quad (17)$$

which also introduces the mapping $\mathbf{q} \rightarrow \mathbf{w}$. After multiplying (15) from the left by \mathbf{w}^T and introducing the conditions of (16), the initial conservation law also expresses the conservation of the mathematical entropy, \mathcal{E} ,

$$\mathcal{E}_t + \vec{\nabla} \cdot \vec{f}^{\mathcal{E}} = 0. \quad (18)$$

Going back to (8), the terms to the left of the equal sign correspond to the Euler equations which, being hyperbolic, add no dissipation and can be reduced to the form (18) with the use of a certain family of entropy functions [9]. The dissipative fluxes at the right hand side of (8) are also modified by the introduction of these entropy variables. We will show in the following sections that both, $\overset{\leftrightarrow}{\mathbf{f}}_v$ and $\overset{\leftrightarrow}{\mathbf{f}}_a$, are symmetrized by this change of variables in the sense that,

$$\overset{\leftrightarrow}{\mathbf{f}}_v = \mathcal{B}_v(\mathbf{q}) \vec{\nabla} \mathbf{w}, \quad \overset{\leftrightarrow}{\mathbf{f}}_a = \mathcal{B}_a(\mathbf{q}) \vec{\nabla} \mathbf{w}, \quad (19)$$

with \mathcal{B}_v and \mathcal{B}_a symmetric matrices. We also define the dissipation introduced by any flux of the form (19) as,

$$D = \left(\vec{\nabla} \mathbf{w} \right)^T \mathcal{B} \vec{\nabla} \mathbf{w}, \quad (20)$$

which will satisfy $D \geq 0$ if \mathcal{B} is positive semi-definite. In this case, after multiplying (8) from the left by \mathbf{w}^T and integrating over Ω , we get a new conservation law for the integrated value of the entropy, $\langle \mathcal{E} \rangle$,

$$\langle \mathcal{E}_t \rangle + \int_{\Omega} \vec{\nabla} \cdot \vec{f}^{\mathcal{E}} dV = \int_{\partial\Omega} \mathbf{w}^T \left(\vec{\mathbf{f}}_v + \vec{\mathbf{f}}_a \right) \cdot \vec{n} dS - \left\langle \vec{\nabla} \mathbf{w}, \vec{\mathbf{f}}_v \right\rangle - \left\langle \vec{\nabla} \mathbf{w}, \vec{\mathbf{f}}_a \right\rangle, \quad (21)$$

that can be further simplified when introducing (19) and (20) into the volume flux terms,

$$\langle \mathcal{E}_t \rangle + \int_{\partial\Omega} \left(\vec{f}^{\mathcal{E}} - \mathbf{w}^T \vec{\mathbf{f}}_v - \mathbf{w}^T \vec{\mathbf{f}}_a \right) \cdot \vec{n} dS = -\langle D_v \rangle - \langle D_a \rangle \leq 0. \quad (22)$$

The last inequality comes from the fact that the dissipation introduced by the viscous and artificial fluxes considered in this work is always positive, as it is explained in Sec. 2.2. Therefore, the entropy remains bounded during the flow evolution at a continuous level. Since the Navier–Stokes equations verify (22), it is desirable to have it satisfied also at a discrete level because entropy stable schemes can be shown to be non-linearly stable [29], and therefore, very robust.

In this work we specifically use two different mathematical entropies:

1. The kinetic energy, $\mathcal{K} = \rho |\vec{u}|^2 / 2$, with entropy variables,

$$\mathbf{w}^{\mathcal{K}} = \frac{\partial \mathcal{K}}{\partial \mathbf{q}} = \left(-\frac{|\vec{u}|^2}{2}, u, v, w, 0 \right)^T. \quad (23)$$

2. The thermodynamic entropy, $\mathcal{S} = -\rho s / (\gamma - 1)$, with $s = \ln p - \gamma \ln \rho$ and,

$$\mathbf{w}^{\mathcal{S}} = \frac{\partial \mathcal{S}}{\partial \mathbf{q}} = \left(\frac{\gamma - s}{\gamma - 1} - \frac{\rho |\vec{u}|^2}{2p}, \frac{\rho u}{p}, \frac{\rho v}{p}, \frac{\rho w}{p}, -\frac{\rho}{p} \right)^T. \quad (24)$$

2.2 Entropy stable dissipation

From (20) and (22) we see that the viscous fluxes are a natural way to introduce dissipation to the entropy equation and thus, we only need to prove that these fluxes are actually adding a positive dissipative term by showing that the matrices \mathcal{B} are positive semi-definite.

This has been already shown for the Navier–Stokes viscous fluxes in [30]. In any case, in this section we complete the previous analysis for the particular cases summarized in Table 1.

Flux type	Kinetic energy	Thermodynamic entropy	μ_α	α_α
Navier–Stokes	✓	✓	constant / LES	–
Guermond–Popov	–	✓	constant	constant

Table 1 Combinations of artificial viscous fluxes and entropy variables used throughout this work.

2.2.1 The kinetic energy variables viscous flux

The Navier–Stokes viscous flux can be expressed in matrix–vector form with $\mathcal{B}_v^K = \mu \mathcal{C}_v^K$ (see Appendix B for the actual definition of the matrix) so, in addition to the physical dissipation, more can be added by augmenting the molecular viscosity, $\mathcal{B}_a^K = \mu_a \mathcal{C}_v^K$. Its associated dissipation is

$$\begin{aligned} D_a^K &= \mu_a \left(\vec{\nabla} \mathbf{w}^K \right)^T \mathcal{C}_v^K \vec{\nabla} \mathbf{w}^K = \mu_a \vec{\nabla} \vec{u} : \left[\left(\vec{\nabla} \vec{u} \right)^T + \vec{\nabla} \vec{u} - \frac{2}{3} \left(\vec{\nabla} \cdot \vec{u} \right) I_3 \right] \\ &= \mu_a \left(2|\mathbf{S}|^2 - \frac{2}{3} \left(\vec{\nabla} \cdot \vec{u} \right)^2 \right) \geq 0. \end{aligned} \quad (25)$$

2.2.2 The thermodynamic entropy variables viscous flux

Since the matrix corresponding to the Navier–Stokes viscous flux is also linearly dependent on ρ with this set of variables, $\mathcal{B}_v^S = \frac{\mu p}{\rho} \tilde{\mathcal{B}}_v^S$, artificial viscosity can also be added by augmenting the molecular viscosity, $\mathcal{B}_a^S = \frac{\mu_a p}{\rho} \tilde{\mathcal{B}}_v^S$. However in this case, the proof for non–linear matrices rests on a Cholesky decomposition of the matrix $\tilde{\mathcal{B}}_a^S = \mathcal{L}_v^{S,T} \mathcal{D}_v^S \mathcal{L}_v^S$, hence,

$$D_a^S = \frac{\mu_a p}{\rho} \vec{\nabla} \mathbf{w}^{S,T} \tilde{\mathcal{B}}_v^S \vec{\nabla} \mathbf{w}^S = \frac{\mu_a p}{\rho} \left(\mathcal{L}_v^S \vec{\nabla} \mathbf{w}^S \right)^T \mathcal{D}_v^S \left(\mathcal{L}_v^S \vec{\nabla} \mathbf{w}^S \right) \geq 0, \quad (26)$$

if all the terms in the diagonal matrix, the artificial viscosity μ_a , and the temperature $T = p/\rho R$ are positive. The diagonal matrix was given in [30],

$$\mathcal{D}_v^S = \text{diag} \left(0, \frac{4}{3}, 1, 1, \frac{\theta p}{\rho}, 0, 0, 1, 1, \frac{\theta p}{\rho}, 0, 0, 0, 0, \frac{\theta p}{\rho} \right), \quad (27)$$

where θ takes the value given in (13). For further information, we include the precise form of the matrices $\tilde{\mathcal{B}}_v^S$ and \mathcal{L}_v^S in Appendix C.

2.2.3 The Guermond–Popov flux

The last flux studied in this work was derived in [19], and introduces two parameters (14). The first one, α_a , introduces dissipation that originates in the continuity equation, proportional to the gradient of the density. This dissipation is carried through the rest of the equations to get an entropy stable dissipation. The second one, μ_a , further introduces dissipation that originates in the momentum equation and whose work is carried to the energy equation, in a similar fashion to the physical dissipation of the Navier–Stokes equations.

To study the dissipation introduced by this flux, it is written in the form $\overset{\leftrightarrow}{\mathbf{f}}_{\text{GP}} = \mathcal{B}_{\text{GP}} \vec{\nabla} \mathbf{w}^S$, using the thermodynamic entropy variables (24). Therefore, the matrix \mathcal{B}_{GP} is written as the sum of the separate contributions of α_a and μ_a

$$\mathcal{B}_{\text{GP}} = \alpha_a \rho \mathcal{B}_{\text{GP}}^\alpha + \mu_a p \mathcal{B}_{\text{GP}}^\mu, \quad (28)$$

where $\mathcal{B}_{\text{GP}}^\alpha$ and $\mathcal{B}_{\text{GP}}^\mu$ are given in Appendix D. As in the Navier–Stokes fluxes, having an entropy stable dissipation rests on the positive–definiteness of (28). In a similar fashion, we perform a Cholesky decomposition of $\mathcal{B}_{\text{GP}} = \mathcal{L}_{\text{GP}}^T \mathcal{D}_{\text{GP}} \mathcal{L}_{\text{GP}}$, with

$$\mathcal{D}_{\text{GP}} = \text{diag} \left(\alpha_a \rho, \mu_a p, \frac{1}{2} \mu_a p, \frac{1}{2} \mu_a p, \alpha_a \rho, \alpha_a \rho, 0, \mu_a p, \frac{1}{2} \mu_a p, \alpha_a \rho, \alpha_a \rho, 0, 0, \mu_a p, \alpha_a \rho \right), \quad (29)$$

thus confirming that

$$D_a^{\text{GP}} = \vec{\nabla} \mathbf{w}^{S,T} \tilde{\mathcal{B}}_{\text{GP}} \vec{\nabla} \mathbf{w} = \left(\mathcal{L}_{\text{GP}} \vec{\nabla} \mathbf{w}^S \right)^T \mathcal{D}_{\text{GP}} \left(\mathcal{L}_{\text{GP}} \vec{\nabla} \mathbf{w}^S \right) \geq 0, \quad (30)$$

as long as $\rho, p \geq 0$. More details of the formulation are given in Appendix D.

2.3 Continuous entropy analysis

We now compute the final expression of the entropy equation (22) for the two entropy variables that we consider. After multiplying (8) by the entropy variables and integrating the result over Ω we get,

$$\langle \mathbf{q}_t, \mathbf{w} \rangle + \left\langle \vec{\nabla} \cdot \overset{\leftrightarrow}{\mathbf{f}}_e, \mathbf{w} \right\rangle = \left\langle \vec{\nabla} \cdot \left(\overset{\leftrightarrow}{\mathbf{f}}_v + \overset{\leftrightarrow}{\mathbf{f}}_a \right), \mathbf{w} \right\rangle. \quad (31)$$

The final form of the different terms depends on the choice of entropy variables. We know from (17) that the first term gives the evolution of the entropy,

$$\langle \mathbf{q}_t, \mathbf{w}^{\mathcal{K}} \rangle = \langle \mathcal{K}_t \rangle, \quad \text{or} \quad \langle \mathbf{q}_t, \mathbf{w}^S \rangle = \langle \mathcal{S}_t \rangle, \quad (32)$$

and also from (16) we can derive that the second term is the integral of the entropy flux over the boundary $\partial\Omega$. However, the case of the kinetic energy needs a special treatment since it does not meet all the requirements set in Sec. 2.1. Specifically, the entropy flux expression (16) is not true and this second term of (31) represents the kinetic energy flux through the boundaries plus a volume term, \mathcal{W}_p , usually associated to the work of the pressure. A more detailed discussion about this term and its role in kinetic energy preserving schemes can be found in [31, 32, 33, 23]. Using (16) to compute the entropy fluxes,

$$\begin{aligned} \left\langle \vec{\nabla} \cdot \overset{\leftrightarrow}{\mathbf{f}}_e, \mathbf{w}^{\mathcal{K}} \right\rangle &= \int_{\partial\Omega} \frac{1}{2} \rho |\vec{u}|^2 \vec{u} \cdot \vec{n} \, dS + \left\langle \vec{u}, \vec{\nabla} p \right\rangle = \int_{\partial\Omega} \vec{f}_e^{\mathcal{K}} \cdot \vec{n} \, dS + \mathcal{W}_p, \\ \left\langle \vec{\nabla} \cdot \overset{\leftrightarrow}{\mathbf{f}}_e, \mathbf{w}^S \right\rangle &= \int_{\partial\Omega} \mathcal{S} \vec{u} \cdot \vec{n} \, dS = \int_{\partial\Omega} \vec{f}_e^{\mathcal{S}} \cdot \vec{n} \, dS, \end{aligned} \quad (33)$$

Finally, the last term gives the dissipative terms after introducing (20) for the physical and artificial viscous fluxes,

$$\left\langle \vec{\nabla} \cdot \left(\overset{\leftrightarrow}{\mathbf{f}}_v + \overset{\leftrightarrow}{\mathbf{f}}_a \right), \mathbf{w} \right\rangle = \int_{\partial\Omega} \mathbf{w}^T \left(\overset{\leftrightarrow}{\mathbf{f}}_v + \overset{\leftrightarrow}{\mathbf{f}}_a \right) \cdot \vec{n} \, dS - \langle D_v \rangle - \langle D_a \rangle. \quad (34)$$

Thus, for both the kinetic energy and thermodynamic entropy we get

$$\langle \mathcal{E}_t \rangle + \int_{\partial\Omega} \vec{f}^{\mathcal{E}} \cdot \vec{n} \, dS + \Theta \mathcal{W}_p + \langle D_v \rangle + \langle D_a \rangle = 0, \quad \vec{f}^{\mathcal{E}} = \vec{f}_e^{\mathcal{E}} - \mathbf{w}^T \left(\overset{\leftrightarrow}{\mathbf{f}}_v + \overset{\leftrightarrow}{\mathbf{f}}_a \right), \quad (35)$$

with $\Theta = 1$ for $\mathcal{E} = \mathcal{K}$, and $\Theta = 0$ for $\mathcal{E} = \mathcal{S}$, which, provided that D_v and D_a are positive, is equivalent to (22) except for the pressure work with kinetic energy entropy variables. We will consider the effect of \mathcal{W}_p in Sec. 5.1, where we perform a semi-discrete entropy stability analysis.

3 Numerical approximation

3.1 Geometrical transformations

The domain Ω is tessellated into non-overlapping hexahedral elements e that are geometrically transformed from a cube $E = [-1, 1]^3$ called the *reference element*. To do that, we define a transfinite mapping from the local $(\vec{\xi} = (\xi, \eta, \zeta)^T \in E)$ to the physical $(\vec{x} = (x, y, z)^T \in e)$ coordinates, $\vec{x} = \vec{X}(\vec{\xi})$. This mapping also relates the differential operators from the physical to the computational space. We also compute the covariant and contravariant basis, and the transformation Jacobian,

$$\vec{a}_i = \frac{\partial \vec{X}}{\partial \xi^i}, \quad J \vec{a}^i = \vec{a}_j \times \vec{a}_k, \quad J = \vec{a}_1 \cdot (\vec{a}_2 \times \vec{a}_3), \quad (i, j, k) \text{ cyclical}, \quad (36)$$

that build the matrix $\mathbf{M} = (J \vec{a}^\xi, J \vec{a}^\eta, J \vec{a}^\zeta)$. This matrix is divergence-free, $\vec{\nabla}_\xi \cdot \mathbf{M} = 0$, which is known as the *metric identities* [34]. With the matrix \mathbf{M} , we transform the gradient and divergence operators [11],

$$J \vec{\nabla} u = \mathbf{M} \vec{\nabla}_\xi u, \quad J \vec{\nabla} \cdot \vec{f} = \vec{\nabla}_\xi \cdot (\mathbf{M}^T \vec{f}) = \vec{\nabla}_\xi \cdot \vec{f}. \quad (37)$$

Next, we construct a block matrix \mathcal{M} from \mathbf{M} using (6). By doing so, we extend the gradient and divergence operators to state and block vectors,

$$J \vec{\nabla} \mathbf{u} = \mathcal{M} \vec{\nabla}_\xi \mathbf{u}, \quad J \vec{\nabla} \cdot \overset{\leftrightarrow}{\mathbf{f}} = \vec{\nabla}_\xi \cdot \left(\mathcal{M}^T \overset{\leftrightarrow}{\mathbf{f}} \right) = \vec{\nabla}_\xi \cdot \overset{\leftrightarrow}{\mathbf{f}}, \quad (38)$$

and we also introduce the matrices \mathbf{M}^T and \mathcal{M}^T as transformation matrices to project covariant space and block vectors into the contravariant frame. We will apply this result throughout this work to express the fluxes in the reference space.

To write the advection–diffusion system (8) in the reference space, it is first casted to a first order system with the definition of the auxiliary variables $\overleftrightarrow{\mathbf{g}} = \overleftrightarrow{\nabla} \mathbf{w}$ (where the gradient is computed from the entropy variables \mathbf{w} (24)). Then these two equations are transformed to the reference space using (38),

$$\begin{aligned} J\mathbf{q}_t + \overleftrightarrow{\nabla}_\xi \cdot \overleftrightarrow{\mathbf{f}}_e(\mathbf{q}) &= \overleftrightarrow{\nabla}_\xi \cdot \left(\overleftrightarrow{\mathbf{f}}_v(\mathbf{q}, \overleftrightarrow{\mathbf{g}}) + \overleftrightarrow{\mathbf{f}}_a(\mathbf{q}, \overleftrightarrow{\mathbf{g}}) \right), \\ J\overleftrightarrow{\mathbf{g}} &= \mathcal{M} \overleftrightarrow{\nabla}_\xi \mathbf{w}. \end{aligned} \quad (39)$$

Finally, we construct two weak forms from (39). We multiply the two equations by two test functions ϕ and $\overleftrightarrow{\varphi}$, we integrate the result over the reference element E, and we use the Gauss law on the divergence and gradients,

$$\begin{aligned} \langle J\mathbf{q}_t, \phi \rangle_E + \int_{\partial E} \phi^T \overleftrightarrow{\mathbf{f}}_e \cdot \hat{n} \, d\hat{S} - \left\langle \overleftrightarrow{\mathbf{f}}_e, \overleftrightarrow{\nabla}_\xi \phi \right\rangle_E \\ = \int_{\partial E} \phi^T \left(\overleftrightarrow{\mathbf{f}}_v + \overleftrightarrow{\mathbf{f}}_a \right) \cdot \hat{n} \, d\hat{S} - \left\langle \overleftrightarrow{\mathbf{f}}_v + \overleftrightarrow{\mathbf{f}}_a, \overleftrightarrow{\nabla}_\xi \phi \right\rangle_E, \\ \left\langle J\overleftrightarrow{\mathbf{g}}, \overleftrightarrow{\varphi} \right\rangle_E = \int_{\partial E} \mathbf{w}^T \overleftrightarrow{\varphi} \cdot \hat{n} \, d\hat{S} - \left\langle \mathbf{w}, \overleftrightarrow{\nabla}_\xi \cdot \overleftrightarrow{\varphi} \right\rangle_E. \end{aligned} \quad (40)$$

In (40), \hat{n} and $d\hat{S}$ are the unit normal vector and the surface differential of the six planar faces of E (e.g. for the faces $\eta = \pm 1$, $\hat{n} = (0, \pm 1, 0)^T$ and $d\hat{S} = d\xi d\zeta$).

3.2 Polynomial approximation

In this work we use a high–order Discontinuous Galerkin Spectral Element Method (DGSEM) [11, 35]. In particular, this work uses the Gauss-Lobatto version of the DGSEM, which makes it possible to construct entropy-stable schemes using the summation-by-parts simultaneous-approximation-term (SBP-SAT) property and two-point entropy–conservative fluxes. Moreover, it handles arbitrary three dimensional curvilinear hexahedral meshes while maintaining high order, spectral accuracy and entropy–stability.

$$\mathbf{q}|_E \approx \mathbf{Q}(\vec{\xi}, t) = \sum_{i,j,k=0}^N \mathbf{Q}_{ijk}(t) l_i(\xi) l_j(\eta) l_k(\zeta). \quad (41)$$

In (41), and following the notation of [36], $l_i(\xi)$ are the Lagrange polynomials associated to the Gauss–Lobatto points, $\{\xi_i, \eta_i, \zeta_i\}_{i,j,k=0}^N$. The coefficients $\mathbf{Q}_{ijk}(t)$ are called the nodal degrees of freedom, whose values coincide with the interpolant evaluation at the GL points, $\mathbf{Q}_{ijk} = \mathbf{Q}(\xi_i, \eta_j, \zeta_k, t)$. Similarly, the fluxes are also represented by their polynomial approximation [11],

$$\overleftrightarrow{\mathbf{f}}|_E \approx \overleftrightarrow{\mathbf{F}}(\vec{\xi}, t) = \sum_{i,j,k=0}^N \overleftrightarrow{\mathbf{F}}_{ijk}(t) l_i(\xi) l_j(\eta) l_k(\zeta), \quad \overleftrightarrow{\mathbf{F}}_{ijk} = \overleftrightarrow{\mathbf{f}}(\mathbf{Q}_{ijk}). \quad (42)$$

The rest of the quantities involved are approximated following (41) and (42), with the exception of the contravariant basis $J\overleftrightarrow{\mathbf{a}}^i$ that build the matrix \mathcal{M} . In the continuous setting, the metric terms satisfy the metric identities, $\overleftrightarrow{\nabla}_\xi \cdot \mathbf{M} = 0$. In its discrete counterpart, the discrete metric identities

represent the ability of the scheme to be free-stream preserving [34], and it is also a requirement for discrete stability [27]. Thus, we follow [34] and use a conservative form of the metrics that ensure the preservation of the metric identities discretely.

We introduce the polynomial approximation in (40),

$$\begin{aligned} \langle \mathcal{J}\mathbf{Q}_t, \phi \rangle_{\mathbf{E}} + \int_{\partial\mathbf{E}} \phi^T \vec{\mathbf{F}}_e \cdot \hat{n} \, d\hat{S} - \left\langle \vec{\mathbf{F}}_e, \vec{\nabla}_\xi \phi \right\rangle_{\mathbf{E}} \\ = \int_{\partial\mathbf{E}} \phi^T \left(\vec{\mathbf{F}}_v + \vec{\mathbf{F}}_a \right) \cdot \hat{n} \, d\hat{S} - \left\langle \left(\vec{\mathbf{F}}_v + \vec{\mathbf{F}}_a \right), \vec{\nabla}_\xi \phi \right\rangle_{\mathbf{E}}, \end{aligned} \quad (43a)$$

$$\left\langle \mathcal{J}\vec{\mathbf{G}}, \vec{\varphi} \right\rangle_{\mathbf{E}} = \int_{\partial\mathbf{E}} \mathbf{W}^T \vec{\varphi} \cdot \hat{n} \, d\hat{S} - \left\langle \mathbf{W}, \vec{\nabla}_\xi \vec{\varphi} \right\rangle_{\mathbf{E}}, \quad (43b)$$

where the test functions are also restricted to N order polynomials in the reference space.

Next, we approximate the exact integrals by quadrature rules. In the reference element $\mathbf{E} = [-1, 1]^3$, the integrals are computed as the product of the nodal degrees of freedom by the quadrature weights $w_i = \int_{-1}^1 l_i(\xi) \, d\xi$ [11],

$$\langle f \rangle_{\mathbf{E}} \approx \langle f \rangle_{\mathbf{E},N} = \sum_{i,j,k=0}^N w_i w_j w_k F_{ijk} = \sum_{i,j,k=0}^N w_{ijk} F_{ijk}. \quad (44)$$

The result is exact if $f \in \mathcal{P}^{2N-1}$. Then, the surface integrals at the boundary $\partial\mathbf{E}$ are also approximated with quadratures. We take into account that the normal vectors at the surfaces $\xi = \pm 1$, $\eta = \pm 1$ and $\zeta = \pm 1$ that make the reference element faces are $\hat{n}_1 = \pm(1, 0, 0)$, $\hat{n}_2 = \pm(0, 1, 0)$ and $\hat{n}_3 = \pm(0, 0, 1)$ to simplify the expressions,

$$\int_{\partial\mathbf{E}} \vec{f} \cdot \hat{n} \, d\hat{S} \approx \int_{\partial\mathbf{E},N} \vec{f} \cdot \hat{n} \, d\hat{S} = \sum_{i,j=0}^N w_i w_j \left(\tilde{F}_{Nij}^\xi - \tilde{F}_{0ij}^\xi + \tilde{F}_{iNj}^\eta - \tilde{F}_{i0j}^\eta + \tilde{F}_{ijN}^\zeta - \tilde{F}_{ij0}^\zeta \right). \quad (45)$$

With Gauss–Lobatto points no additional projection is required and one only chooses the appropriate nodal degree of freedom that corresponds to a given surface node (e.g. $\mathbf{Q}(1, \eta_j, \zeta_k) = \mathbf{Q}_{Njk}$). The latter, alongside the exactness of the quadrature, makes the scheme satisfy the discrete Gauss law [37],

$$\left\langle \vec{\tilde{F}}, \vec{\nabla}_\xi G \right\rangle_{\mathbf{E},N} = \int_{\partial\mathbf{E},N} G \vec{\tilde{F}} \cdot \hat{n} \, d\hat{S} - \left\langle \vec{\nabla}_\xi \cdot \vec{\tilde{F}}, G \right\rangle_{\mathbf{E},N}. \quad (46)$$

This is a direct consequence of the aforementioned SBP derivative operator [38, 39, 30, 40] that, when expressed in matrix form, D , has the properties,

$$PD = Q, \quad P = P^T, \quad Q + Q^T = B, \quad B = e_N e_N^T - e_0 e_0^T, \quad (47)$$

where P is a diagonal matrix with the quadrature weights and e_i are column vectors filled with zeros except for position i . Equation (47) is simply the matrix form of (46) for SBP operators.

As a final remark, it is possible to write surface integrals both in computational or physical coordinates. The matrix \mathcal{M} relates the normal unit vector and surface differentials, $\vec{n} \, dS = \mathcal{M} \cdot \hat{n} \, d\hat{S}$. Hence, we can write,

$$\int_{\partial\mathbf{E},N} \vec{\tilde{F}} \cdot \hat{n} \, d\hat{S} = \int_{\partial e,N} \vec{\tilde{F}} \cdot \vec{n} \, dS. \quad (48)$$

The representation in physical coordinates is convenient because at the interface between two elements, e^+ and e^- , the normal vectors satisfy $\vec{n}^+ dS^+ = -\vec{n}^- dS^-$.

We approximate the integrals in (43) with quadratures, and use (48) to get

$$\begin{aligned} \langle \mathcal{J}\mathbf{Q}_t, \phi \rangle_{E,N} &+ \int_{\partial e,N} \phi^T \mathbf{F}_e^{\leftrightarrow*} \cdot \vec{n} dS - \left\langle \mathbf{F}_e^{\leftrightarrow}, \vec{\nabla}_\xi \phi \right\rangle_{E,N} \\ &= \int_{\partial e,N} \phi^T \left(\mathbf{F}_v^{\leftrightarrow*} + \mathbf{F}_a^{\leftrightarrow*} \right) \cdot \vec{n} dS - \left\langle \mathbf{F}_v^{\leftrightarrow} + \mathbf{F}_a^{\leftrightarrow}, \vec{\nabla}_\xi \phi \right\rangle_{E,N}, \end{aligned} \quad (49a)$$

$$\left\langle \mathcal{J}\mathbf{G}, \vec{\varphi} \right\rangle_{E,N} = \int_{\partial e,N} \mathbf{W}^{*,T} \vec{\varphi} \cdot \vec{n} dS - \left\langle \mathbf{W}, \vec{\nabla}_\xi \cdot \vec{\varphi} \right\rangle_{E,N}. \quad (49b)$$

In (49), we have replaced the interface fluxes by the uniquely defined *numerical fluxes* that depend on the two adjacent states [11]. These are detailed in Sec. 3.3.

Finally, we use a split-form scheme for the inviscid fluxes. The split-form method allows us to obtain schemes that are entropy stable discretely through the use of a two-point volume flux function [30]. Thus, we apply the discrete Gauss law on the inviscid fluxes of (49a),

$$\begin{aligned} \langle \mathcal{J}\mathbf{Q}_t, \phi \rangle_{E,N} &+ \int_{\partial e,N} \phi^T \left(\mathbf{F}_e^{\leftrightarrow*} - \mathbf{F}_e^{\leftrightarrow} \right) \cdot \vec{n} dS + \left\langle \vec{\nabla}_\xi \cdot \mathbf{F}_e^{\leftrightarrow}, \phi \right\rangle_{E,N} \\ &= \int_{\partial e,N} \phi^T \left(\mathbf{F}_v^{\leftrightarrow*} + \mathbf{F}_a^{\leftrightarrow*} \right) \cdot \vec{n} dS - \left\langle \mathbf{F}_v^{\leftrightarrow} + \mathbf{F}_a^{\leftrightarrow}, \vec{\nabla}_\xi \phi \right\rangle_{E,N}, \end{aligned} \quad (50)$$

and compute the divergence with a two-point volume flux function $\mathbf{F}^{\leftrightarrow\#}(\mathbf{Q}_{ijk}, \mathbf{Q}_{nml})$,

$$\left(\vec{\nabla}_\xi \cdot \mathbf{F}_e^{\leftrightarrow} \right)_{ijk} \approx \mathbb{D} \left(\mathbf{F}_e^{\leftrightarrow\#} \right)_{ijk} = 2 \sum_{n=0}^N \left(D_{in} \mathbf{F}^{\leftrightarrow\#,1}(\mathbf{Q}_{ijk}, \mathbf{Q}_{njk}) + D_{jn} \mathbf{F}^{\leftrightarrow\#,2}(\mathbf{Q}_{ijk}, \mathbf{Q}_{ink}) + D_{kn} \mathbf{F}^{\leftrightarrow\#,3}(\mathbf{Q}_{ijk}, \mathbf{Q}_{ijn}) \right). \quad (51)$$

where $D_{ij} = l'_j(\xi_i)$. The interested reader can find the details on [33]. Throughout this work, two different two-point volume flux functions will be used. For kinetic energy preserving schemes, we use the two-point flux by Pirozzoli [41], whereas for thermodynamic entropy stable schemes we use the two-point flux by Chandrashekar [42]. With the two-point divergence, the DG scheme (50) is

$$\begin{aligned} \langle \mathcal{J}\mathbf{Q}_t, \phi \rangle_{E,N} &+ \int_{\partial e,N} \phi^T \left(\mathbf{F}_e^{\leftrightarrow*} - \mathbf{F}_e^{\leftrightarrow} \right) \cdot \vec{n} dS + \left\langle \mathbb{D} \left(\mathbf{F}_e^{\leftrightarrow\#} \right), \phi \right\rangle_{E,N} \\ &= \int_{\partial e,N} \phi^T \left(\mathbf{F}_v^{\leftrightarrow*} + \mathbf{F}_a^{\leftrightarrow*} \right) \cdot \vec{n} dS - \left\langle \mathbf{F}_v^{\leftrightarrow} + \mathbf{F}_a^{\leftrightarrow}, \vec{\nabla}_\xi \phi \right\rangle_{E,N}, \end{aligned} \quad (52a)$$

$$\left\langle \mathcal{J}\mathbf{G}, \vec{\varphi} \right\rangle_{E,N} = \int_{\partial e,N} \mathbf{W}^{*,T} \vec{\varphi} \cdot \vec{n} dS - \left\langle \mathbf{W}, \vec{\nabla}_\xi \cdot \vec{\varphi} \right\rangle_{E,N}. \quad (52b)$$

Recall at this point that the flux $\mathbf{F}_a^{\leftrightarrow}$ represents the additional viscosity added by either the molecular viscosity $\mathbf{F}_a^{\leftrightarrow} = \mathbf{F}_v^{\leftrightarrow}(\mu_a)$ or the Guermond–Popov fluxes $\mathbf{F}_a^{\leftrightarrow} = \mathbf{F}_{\text{GP}}^{\leftrightarrow}(\alpha_a, \mu_a)$.

3.3 Intercell numerical fluxes

One of the characteristics that make DG schemes attractive is that they can introduce dissipation at the inter–element faces. The characteristics of this dissipation are dictated by the choice of numerical fluxes $\overset{\leftrightarrow}{\mathbf{F}}_e$, $\overset{\leftrightarrow}{\mathbf{F}}_v$ and $\overset{\leftrightarrow}{\mathbf{F}}_a$. We write the one–dimensional numerical fluxes, which are later transformed to three–dimensions using the rotational invariance property [7],

$$\mathbf{F}_e^* \cdot \vec{n} = \underline{\mathbb{T}}^T \mathbf{F}_e^{1,*}(\mathbf{Q}_{nL}, \mathbf{Q}_{nR}), \quad \mathbf{Q}_n = \underline{\mathbb{T}}\mathbf{Q}, \quad \underline{\mathbb{T}} = \begin{pmatrix} 1 & 0 & 0 & 0 & 0 \\ 0 & n_x & n_y & n_z & 0 \\ 0 & t_{1,x} & t_{1,y} & t_{1,z} & 0 \\ 0 & t_{2,x} & t_{2,y} & t_{2,z} & 0 \\ 0 & 0 & 0 & 0 & 1 \end{pmatrix}, \quad (53)$$

where \vec{n} , \vec{t}_1 and \vec{t}_2 are the three vectors that define the local reference frame at a point of the interface. For the inviscid fluxes, one can construct entropy conserving schemes (i.e. without numerical dissipation) using the two–point flux as a numerical flux,

$$\overset{\leftrightarrow}{\mathbf{F}}_e(\mathbf{Q}_L, \mathbf{Q}_R) \cdot \vec{n} = \underline{\mathbb{T}}^T \overset{\leftrightarrow}{\mathbf{F}}_e^{1,\#}(\mathbf{Q}_{nL}, \mathbf{Q}_{nR}), \quad (54)$$

or construct an entropy stable (dissipative) approximation by adding extra terms to it. For the latter, there are several choices available, which depend on whether one constructs a kinetic energy preserving or a thermodynamic entropy stable scheme [42]. For kinetic energy consistency (e.g. Pirozzoli’s), the Lax–Friedrichs numerical flux is stable [33]

$$\mathbf{F}_e^*(\mathbf{Q}_{nL}, \mathbf{Q}_{nR}) \cdot \vec{n} = \underline{\mathbb{T}}^T \left(\mathbf{F}_e^{1,\#}(\mathbf{Q}_{nL}, \mathbf{Q}_{nR}) - \frac{1}{2} |\lambda_{\max}| \llbracket \mathbf{Q}_n \rrbracket \right), \quad \llbracket \mathbf{Q} \rrbracket = \mathbf{Q}_R - \mathbf{Q}_L, \quad (55)$$

and for the thermodynamic entropy (e.g. Chandrashekar’s), a popular choice is to construct a matrix dissipation flux based on Roe’s Riemann solver [42],

$$\mathbf{F}_e^*(\mathbf{Q}_{nL}, \mathbf{Q}_{nR}) \cdot \vec{n} = \underline{\mathbb{T}}^T \left(\mathbf{F}_e^{1,\#}(\mathbf{Q}_{nL}, \mathbf{Q}_{nR}) - \frac{1}{2} \underline{\mathbb{M}} \llbracket \mathbf{W}_n \rrbracket \right), \quad (56)$$

where the positive definite matrix $\underline{\mathbb{M}}$ depends on the two states and is constructed from the eigenvectors and the absolute value of the eigenvalues of the Euler equations.

For the entropy variables, viscous fluxes, and artificial viscosity, we follow [27] and use the Bassi–Rebay 1 (BR1) scheme [43],

$$\mathbf{W}^* = \{\{\mathbf{W}\}\}, \quad \overset{\leftrightarrow}{\mathbf{F}}_v^* = \{\{\overset{\leftrightarrow}{\mathbf{F}}_v\}\}, \quad \overset{\leftrightarrow}{\mathbf{F}}_a^* = \{\{\overset{\leftrightarrow}{\mathbf{F}}_a\}\}. \quad (57)$$

3.4 Physical boundaries numerical fluxes

The boundary conditions are weakly enforced through numerical fluxes applied to the interior state and to a ghost state constructed from the boundary data. In this work, we use free– and no–slip adiabatic walls, inflow, and outflow boundary conditions. The implementation of the adiabatic wall boundary conditions is entropy stable, while inflow and outflow boundaries can increase and/or decrease the entropy.

3.4.1 Adiabatic wall

For the inviscid fluxes, both free– and no–slip walls cancel the normal velocity. This enforcement is done through the numerical flux, after the construction of a mirrored ghost state with negative normal velocity,

$$\mathbf{Q}_{n,\text{ghost}} = (\rho, -\rho U, \rho V, \rho W, \rho E)^T, \quad \overset{\leftrightarrow}{\mathbf{F}}_e \cdot \vec{n} = \overset{\leftrightarrow}{\mathbf{F}}_e(\mathbf{Q}_n, \mathbf{Q}_{n,\text{ghost}}) \cdot \vec{n} \quad (58)$$

For the viscous fluxes, the free–slip adiabatic wall cancels the stress tensor and the heat flux at the wall, thus we enforce Neumann boundary conditions in the state variables,

$$\mathbf{W}_n^* = \mathbf{W}_n, \quad \overset{\leftrightarrow}{\mathbf{F}}_v \cdot \vec{n} = 0. \quad (59)$$

No–slip adiabatic walls, on the contrary, are of Dirichlet type for the three velocities and Neumann for the energy,

$$\mathbf{W}_n^* = (W_{1n}, 0, 0, 0, W_{5n})^T, \quad \overset{\leftrightarrow}{\mathbf{F}}_v \cdot \vec{n} = (0, F_{v,2}, F_{v,3}, F_{v,4}, 0)^T. \quad (60)$$

For the Guermond–Popov fluxes, we cancel the flux at the physical boundary for the first and fifth equations, and use either Dirichlet boundary conditions at no–slip walls, ($F^* = F, W^* = 0$) or Neumann boundary conditions at free–slip walls ($F^* = 0, W^* = W$) for the momentum equations,

$$\mathbf{W}_n^* = (W_{1n}, W_{2n}^*, W_{3n}^*, W_{4n}^*, W_{5n})^T, \quad \overset{\leftrightarrow}{\mathbf{F}}_{\text{GP}} \cdot \vec{n} = (0, F_{\text{GP},2}^*, F_{\text{GP},3}^*, F_{\text{GP},4}^*, 0)^T. \quad (61)$$

3.4.2 Supersonic inflow

Inflow boundary conditions at supersonic velocities only carry information from the exterior into the domain and thus, they can be imposed in the inviscid term by setting a ghost state with the boundary values and using inter–element fluxes to couple it with the interior solution,

$$\mathbf{Q}_{n,\text{ghost}} = (\rho_0, \rho_0 U_0, \rho_0 V_0, \rho_0 W_0, \rho_0 E_0)^T. \quad (62)$$

For the viscous fluxes we use Neumann boundary conditions and cancel the viscous stress as done for free–slip walls.

3.4.3 Outflow

Since information travels upstream only in subsonic flows, the value of the pressure at the boundary for the inviscid flux is imposed through ghost states only for this case, whereas it takes the value of the interior if the local Mach number is greater than one,

$$\begin{aligned} \mathbf{Q}_{n,\text{ghost}} &= (\rho, \rho U, \rho V, \rho W, \rho E)^T, & \text{if } M > 1, \\ \mathbf{Q}_{n,\text{ghost}} &= (\rho_0, \rho_0 U_0, \rho_0 V_0, \rho_0 W_0, \rho_0 E_0)^T, & \text{if } M \leq 1, \end{aligned} \quad (63)$$

where we compute the exterior values from the Riemann invariants,

$$\begin{aligned}\rho_0 &= \rho \left(1 + \frac{p_0/p - 1}{\gamma} \right), \\ \vec{U}_0 &= \vec{U}_t + \vec{U}_{0,n}, \\ \vec{U}_{0,n} &= r^+ - \frac{2a_0}{\gamma - 1}, \quad r^+ = \vec{U}_n + \frac{2a}{\gamma - 1},\end{aligned}\tag{64}$$

being \vec{U}_n and \vec{U}_t the normal and tangent velocity vectors. As for the viscous fluxes, we again use Neumann boundary conditions with no viscous stress, and the entropy variables at the outlet use the values of the interior points. For more details, see [44, 45].

4 Spectral vanishing viscosity: filtered artificial dissipation

In this section we introduce the construction of an entropy stable spectral vanishing viscosity that helps us to modulate the dissipation by spatially filtering the artificial viscosity fluxes. The SVV approach was first considered by Tadmor [46], where he added a filtered viscous term to the Burgers' equation,

$$\frac{\partial U}{\partial t} + \frac{1}{2} \frac{\partial U^2}{\partial x} = \varepsilon \frac{\partial}{\partial x} \left[\mathcal{F} \star \frac{\partial U}{\partial x} \right], \quad \varepsilon \sim \frac{1}{N^\beta \log N}, \quad \beta < 1.\tag{65}$$

In this work we use Legendre polynomials, $L_k(x)$, as a modal basis, where k not only indicates the mode number but also serves as a measure of the wavenumber. In this case, the filtering operator, \star , can be expressed as an element-wise product where, for each mode, L_k , there is a filter kernel coefficient, \mathcal{F}_k , that modulates its intensity. Under this assumptions, Tadmor proved that the solution converges to the weak solution that is also physically plausible. However, there is not only one possible shape for this filter kernel and different options have been proposed. For instance, in [46] it is defined as,

$$\hat{\mathcal{F}}_k = \begin{cases} 0, & k \leq M \\ 1, & k > M, \end{cases} \quad \varepsilon M = 0.25,\tag{66}$$

or, in [47, 48], a C^∞ function is used to improve the resolution,

$$\hat{\mathcal{F}}_k = \begin{cases} 0, & k \leq M \\ \exp \left[-\frac{(k - N)^2}{(k - M)^2} \right], & k > M, \end{cases} \quad M \approx 5\sqrt{N}.\tag{67}$$

Finally, taking advantage of the fact that the viscosity varies for the different frequencies considered by the solution approximation, we can also use it to add more dissipation in turbulent, unresolved regions, where the one from the underlying numerical scheme is not enough. This approach was followed in [20, 21] and it can also be combined with other LES methods, as in [25, 26].

We first establish the foundation in one dimension, and then extend the methodology to the three-dimensional curvilinear setting. We also define the reference line $L = [-1, 1]$, face $F = [-1, 1]^2$ and element $E = [-1, 1]^3$.

4.1 Polynomial filtering: one dimension

In the nodal DG method, the solution approximated by degree N polynomials is represented using the Lagrange polynomials,

$$Q(\xi) = \sum_{j=0}^N Q_j l_j(\xi), \quad (68)$$

but other representations are also possible. Precisely, we are interested in a modal reconstruction since it provides a natural approach to polynomial filtering, as we can directly manipulate the intensity of each polynomial mode. We introduce the Legendre polynomials, $L_j(\xi)$, to represent the solution,

$$Q(\xi) = \sum_{j=0}^N Q_j l_j(\xi) = \sum_{j=0}^N \hat{Q}_j L_j(\xi), \quad (69)$$

where \hat{Q}_j are the modal coefficients of the solution (as opposed to the nodal coefficients, Q_j).

The Legendre polynomials are an orthogonal basis (both continuously and discretely) since they satisfy,

$$\langle L_n, L_m \rangle_{L,N} = \|L_n\|_N^2 \delta_{nm}. \quad (70)$$

Note that all the norms $\|L_n\|_N$ are exactly computed with quadratures (i.e. they involve a quadrature of degree less than $2N - 1$) except for the one associated to the highest mode, $\|L_N\|_N$. The exactness of the norm is not essential however, as long as it is positive.

We define a *forward* (F) operation that computes the modal coefficients from the nodal quantities. To do that, we multiply (69) by one of the Legendre polynomials $L_i(\xi)$ and compute its quadrature over L ,

$$\langle Q, L_i \rangle_{L,N} = \sum_{j=0}^N Q_j \langle l_j, L_i \rangle_{L,N} = \sum_{j=0}^N \hat{Q}_j \langle L_j, L_i \rangle_{L,N} = \|L_i\|_N^2 \hat{Q}_i, \quad (71)$$

therefore,

$$\hat{Q}_i = \sum_{j=0}^N \frac{\langle l_j, L_i \rangle}{\|L_i\|^2} Q_j = \sum_{j=0}^N F_{ij} Q_j, \quad F_{ij} = \frac{\langle l_j, L_i \rangle}{\|L_i\|^2}. \quad (72)$$

Similarly, the *backward* (B) operation recovers the nodal coefficients from the modal form. In this case, we multiply (69) by one of the Lagrange polynomials, $l_i(\xi)$ and compute its quadrature over L ,

$$\langle Q, l_i \rangle_{L,N} = \sum_{j=0}^N Q_j \langle l_j, l_i \rangle_{L,N} = w_i Q_i = \sum_{j=0}^N \hat{Q}_j \langle L_j, l_i \rangle_{L,N}, \quad (73)$$

and therefore,

$$Q_i = \sum_{j=0}^N \frac{\langle L_j, l_i \rangle_{L,N}}{w_i} \hat{Q}_j = \sum_{j=0}^N B_{ij} \hat{Q}_j, \quad B_{ij} = \frac{\langle L_j, l_i \rangle_{L,N}}{w_i}. \quad (74)$$

This two transformations and its associated matrices, F and B , satisfy two properties required for the stability of the scheme.

Property 1 They are inverse matrices, $FB = BF = I$, as the direct multiplication shows,

$$\begin{aligned}
(FB)_{ij} &= \sum_{k=0}^N F_{ik} B_{kj} = \sum_{k=0}^N \frac{\langle L_i, l_k \rangle_{L,N}}{\|L_i\|_N^2} \frac{\langle l_k, L_j \rangle_{L,N}}{w_k} \\
&= \sum_{k=0}^N \frac{1}{w_k \|L_i\|_N^2} \sum_{l=0}^N w_l^2 L_i(\xi_l) L_j(\xi_l) l_k^2(\xi_l) \\
&= \frac{1}{\|L_i\|_N^2} \sum_{k=0}^N w_k L_i(\xi_k) L_j(\xi_k) = \frac{\langle L_i, L_j \rangle_{L,N}}{\|L_i\|_N^2} = \delta_{ij}
\end{aligned} \tag{75}$$

Property 2 Multiplied by the discrete nodal and modal weights, they are transposed matrices,

$$w_i B_{ij} = \|L_j\|_N^2 F_{ji}. \tag{76}$$

Properties 1 and 2 allow us to relate the discrete norms in both nodal and modal spaces (Parseval's identity),

Property 3 Discrete Parseval's identity: discrete inner products can be equivalently computed from nodal or modal coefficients

$$\langle U, V \rangle_{L,N} = \sum_{i=0}^N w_i U_i V_i = \sum_{j=0}^N \|L_j\|_N^2 \hat{U}_j \hat{V}_j. \tag{77}$$

The proof for this property uses Properties 1 (at the second equality) and 2 (at the fourth equality),

$$\begin{aligned}
\langle U, V \rangle_{L,N} &= \sum_{i=0}^N w_i U_i V_i = \sum_{i=0}^N w_i U_i \sum_{j,k=0}^N B_{ij} F_{jk} V_k = \sum_{i,j=0}^N U_i (w_i B_{ij}) \sum_{k=0}^N F_{jk} V_k \\
&= \sum_{i,j=0}^N U_i \|L_j\|_N^2 F_{ji} \hat{V}_j = \sum_{j=0}^N \|L_j\|_N^2 \hat{V}_j \sum_{i=0}^N F_{ji} U_i = \sum_{j=0}^N \|L_j\|_N^2 \hat{U}_j \hat{V}_j.
\end{aligned} \tag{78}$$

The ability to compute equivalent discrete L^2 norms either from the nodal or modal spaces is key to show the discrete stability of filtered dissipative fluxes.

In this work, we locally filter the polynomial functions by applying a given filter kernel according to,

$$\mathcal{F}(\xi) = \sum_{j=0}^N \hat{\mathcal{F}}_j L_j(\xi). \tag{79}$$

In the case of the solution vector, Q , the application of the filter kernel returns another polynomial whose modal coefficients are the point-wise product of the modal coefficients of \mathcal{F} and Q ,

$$\bar{Q} = \mathcal{F} \star Q = \sum_{j=0}^N \hat{\mathcal{F}}_j \hat{Q}_j L_j(\xi). \tag{80}$$

Thus we get the filtered solution \bar{Q} in the modal space, which is then returned to a nodal representation, \bar{Q}_i , afterwards. For computational efficiency, we can define a single matrix–vector product operation that encapsulates the forward, filtering, and backwards steps,

$$\bar{Q}_i = \sum_{j=0}^N \mathcal{H}_{ij} Q_j, \quad \mathcal{H} = B \text{diag} \left(\hat{\mathcal{F}} \right) F. \quad (81)$$

The next theorem, also used similarly in [49], will prove to be fundamental for entropy stability,

Theorem 1 *The inner product of Q and \bar{Q} is positive (assuming positive filtering coefficients $\hat{\mathcal{F}}_i$),*

$$\langle Q, \bar{Q} \rangle_{L,N} = \langle Q, \mathcal{F} \star Q \rangle_{L,N} \geq 0. \quad (82)$$

Proof Using Property 3, the inner product of Q and \bar{Q} can be expressed in modal space where, according to (80),

$$\bar{Q} = \sum_{i=0}^N \hat{Q}_i L_i, \quad \hat{Q}_i = \hat{\mathcal{F}}_i Q_i. \quad (83)$$

Introducing this definition into the inner product in (82),

$$\langle Q, \bar{Q} \rangle_{L,N} = \sum_{j=0}^N \|L_j\|^2 \hat{Q}_j \hat{Q}_j = \sum_{j=0}^N \|L_j\|^2 \hat{\mathcal{F}}_j \hat{Q}_j^2, \quad (84)$$

which is positive as long as the filter kernel coefficients are positive. \square

4.2 Polynomial filtering: three dimensions

In three dimensions, the polynomial framework is constructed from a tensor product form of the one-dimensional one. Therefore, it automatically inherits the properties described for the one-dimensional space in Sec. 4.1.

We get the modal representation of a solution,

$$\mathbf{Q} = \sum_{i,j,k=0}^N \mathbf{Q}_{ijk} l_i(\xi) l_j(\eta) l_k(\zeta) = \sum_{i,j,k} \hat{\mathbf{Q}}_{ijk} L_i(\xi) L_j(\eta) L_k(\zeta), \quad (85)$$

from a weak-form with the tensor product Legendre polynomials $L_{ijk} = L_i(\xi) L_j(\eta) L_k(\zeta)$,

$$\langle \mathbf{Q}, L_{ijk} \rangle_{E,N} = \sum_{m,n,l=0}^N \mathbf{Q}_{mnl} \langle l_{mnl}, L_{ijk} \rangle_{E,N} = \sum_{m,n,l=0}^N \hat{\mathbf{Q}}_{mnl} \langle L_{mnl}, L_{ijk} \rangle_{E,N}. \quad (86)$$

The tensor product inner products in the three-dimensional reference element E reduce to the product of the inner products in the reference line L ,

$$\langle l_{mnl}, L_{ijk} \rangle_{E,N} = \langle l_m, L_i \rangle_{L,N} \langle l_n, L_j \rangle_{L,N} \langle l_l, L_k \rangle_{L,N}. \quad (87)$$

Then, we get the modal coefficients from three matrix–vector multiplications with the one–dimensional *forward* matrix F in each of the local coordinates directions,

$$\hat{\mathbf{Q}}_{ijk} = \sum_{m,n,l=0}^N \frac{\langle l_m, L_i \rangle_{L,N}}{\|L_i\|_N^2} \frac{\langle l_n, L_j \rangle_{L,N}}{\|L_j\|_N^2} \frac{\langle l_l, L_k \rangle_{L,N}}{\|L_k\|_N^2} \mathbf{Q}_{mnl} = \sum_{m,n,l=0}^N F_{im} F_{jn} F_{kl} \mathbf{Q}_{mnl} \quad (88)$$

Theorem 2 *Parseval's discrete identity: the three–dimensional framework also satisfies a discrete version of Parseval's identity,*

$$\langle \mathbf{U}, \mathbf{V} \rangle_{E,N} = \sum_{i,j,k=0}^N w_{ijk} \mathbf{U}_{ijk}^T \mathbf{V}_{ijk} = \sum_{i,j,k=0}^N \|L_i\|_N^2 \|L_j\|_N^2 \|L_k\|_N^2 \hat{\mathbf{U}}_{ijk}^T \hat{\mathbf{V}}_{ijk}. \quad (89)$$

Proof We start by defining a partial modal transformation as the result of performing the transformation to the modal space only in one direction,

$$\hat{\mathbf{Q}}_{ijk}^\xi = \sum_{m=0}^N F_{im} \mathbf{Q}_{mjk}, \quad \hat{\mathbf{Q}}_{ijk}^\eta = \sum_{m=0}^N F_{jm} \mathbf{Q}_{imk}, \quad \hat{\mathbf{Q}}_{ijk}^\zeta = \sum_{m=0}^N F_{km} \mathbf{Q}_{ijm}, \quad (90)$$

which can be applied recursively in two,

$$\hat{\mathbf{Q}}_{ijk}^{\xi^i \xi^j} = \widehat{\hat{\mathbf{Q}}_{ijk}^{\xi^i}}^{\xi^j}, \quad (91)$$

and three directions,

$$\hat{\mathbf{Q}}_{ijk}^{\xi\eta\zeta} = \hat{\mathbf{Q}}_{ijk}. \quad (92)$$

Expressing the inner product of (89) in nodal space, and applying Property 3 in each direction at a time,

$$\begin{aligned} \langle \mathbf{U}, \mathbf{V} \rangle_{E,N} &= \sum_{i,j,k=0}^N w_{ijk} \mathbf{U}_{ijk}^T \mathbf{V}_{ijk} = \sum_{i,j,k=0}^N \|L_i\|_N^2 w_{jk} \hat{\mathbf{U}}_{ijk}^{\xi,T} \hat{\mathbf{V}}_{ijk}^\xi \\ &= \sum_{i,j,k=0}^N \|L_i\|_N^2 \|L_j\|_N^2 w_k \hat{\mathbf{U}}_{ijk}^{\xi\eta,T} \hat{\mathbf{V}}_{ijk}^{\xi\eta} \\ &= \sum_{i,j,k=0}^N \|L_i\|_N^2 \|L_j\|_N^2 \|L_k\|_N^2 \hat{\mathbf{U}}_{ijk}^T \hat{\mathbf{V}}_{ijk}, \end{aligned} \quad (93)$$

which is the equivalent of Property 3 in three dimensions. \square

In three dimensions, the polynomials are also locally filtered as,

$$\bar{\mathbf{Q}} = \mathcal{F} \star \mathbf{Q} = \sum_{i,j,k=0}^N \hat{\mathcal{F}}_{ijk} \hat{\mathbf{Q}}_{ijk} L_i(\xi) L_j(\eta) L_k(\zeta). \quad (94)$$

For the most general filter kernel with coefficients $\hat{\mathcal{F}}_{ijk}$,

$$\bar{\mathbf{Q}}_{ijk} = \sum_{m,n,l=0}^N \sum_{p,q,r=0}^N B_{ip} B_{jq} B_{kr} \hat{\mathcal{F}}_{pqr} F_{pm} F_{qn} F_{rl} \mathbf{Q}_{mnl}, \quad (95)$$

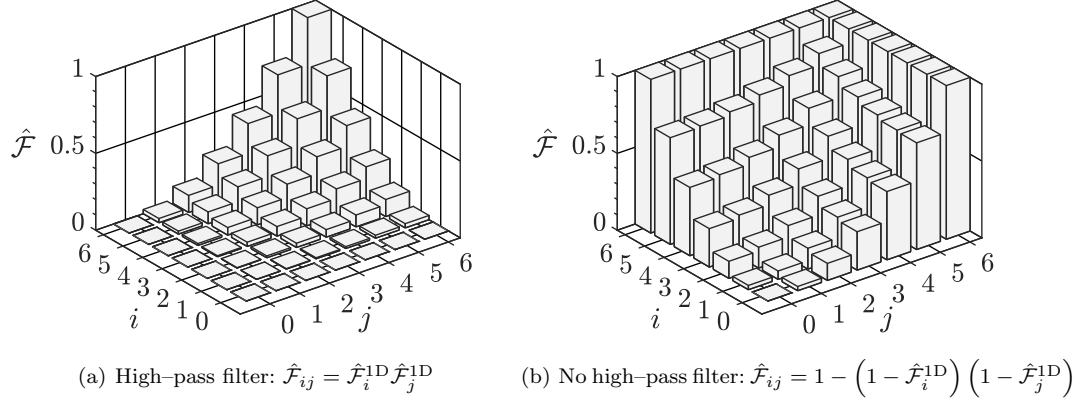


Fig. 1 Design of multidimensional filters from the tensor product of a one-dimensional filter. Two options are provided: a high-pass filter, where for example $\hat{\mathcal{F}}_{Nj} = \hat{\mathcal{F}}_j^{1D}$, and a non high-pass version, where $\hat{\mathcal{F}}_{Nj} = 1$. Recall that modes with high filter coefficient values are more dissipated. For this plot, $N = 6$ and $\hat{\mathcal{F}}_i^{1D} = (i/N)^2$

we get a fully three-dimensional tensor product (i.e. with $(N+1)^3$ operations). However, computations are drastically reduced if we restrict ourselves to a tensor product version of the filter, $\hat{\mathcal{F}}_{ijk} = \hat{\mathcal{F}}_i \hat{\mathcal{F}}_j \hat{\mathcal{F}}_k$, which reduces the filtering to three one-dimensional matrix-vector multiplications (i.e. $3(N+1)$ operations),

$$\bar{\mathbf{Q}}_{ijk} = \sum_{m,n,l=0}^N \mathcal{H}_{im} \mathcal{H}_{jn} \mathcal{H}_{kl} \mathbf{Q}_{mnl} = \sum_{m=0}^N \mathcal{H}_{im} \sum_{n=0}^N \mathcal{H}_{jn} \sum_{l=0}^N \mathcal{H}_{kl} \mathbf{Q}_{mnl}, \quad \mathcal{H} = B\hat{\mathcal{F}}F. \quad (96)$$

The methodology presented here is valid for any positive filtering functions $\hat{\mathcal{F}}_{ijk}$. However, we only present numerical results for the tensor product filter $\hat{\mathcal{F}}_{ijk} = \hat{\mathcal{F}}_i \hat{\mathcal{F}}_j \hat{\mathcal{F}}_k$. The matrix \mathcal{H} is that defined for the one-dimensional filtering. From one-dimensional filters, $\hat{\mathcal{F}}_i^{1D}$, we can construct the three dimension version in a high-pass version, Fig. 1(a),

$$\hat{\mathcal{F}}_{ijk} = \hat{\mathcal{F}}_i^{1D} \hat{\mathcal{F}}_j^{1D} \hat{\mathcal{F}}_k^{1D}, \quad (97)$$

or in a non high-pass version, Fig. 1(b),

$$\hat{\mathcal{F}}_{ijk} = 1 - (1 - \hat{\mathcal{F}}_i^{1D})(1 - \hat{\mathcal{F}}_j^{1D})(1 - \hat{\mathcal{F}}_k^{1D}). \quad (98)$$

Finally, we extend Theorem 1 to three dimensions,

Property 4 *The inner product of the filtered state vector $\bar{\mathbf{Q}}$ and the state vector \mathbf{Q} is positive. We compute the inner product in the modal coefficients,*

$$\langle \mathbf{Q}, \bar{\mathbf{Q}} \rangle_{E,N} = \sum_{i,j,k=0}^N \|L_i\|_N^2 \|L_j\|_N^2 \|L_k\|_N^2 \hat{\mathbf{Q}}_{ijk} \hat{\mathbf{Q}}_{ijk} = \sum_{i,j,k=0}^N \|L_i\|_N^2 \|L_j\|_N^2 \|L_k\|_N^2 \hat{\mathcal{F}}_{ijk} \hat{\mathbf{Q}}_{ijk}^2 \geq 0, \quad (99)$$

that we can represent as,

$$\langle \mathbf{Q}, \bar{\mathbf{Q}} \rangle_{E,N} = \langle \mathbf{Q}, \mathcal{F} \star \mathbf{Q} \rangle_{E,N} \geq 0. \quad (100)$$

5 Entropy stable filtered dissipation

We now apply the findings in Sec. 4 to construct entropy stable filtered dissipative fluxes for the Navier–Stokes equations. Depending on the form of the fluxes, $\overset{\leftrightarrow}{\mathbf{F}}_a = \mathcal{B}_a(\mathbf{Q})\overset{\leftrightarrow}{\mathbf{G}}$, we proceed differently:

1. \mathcal{B}_a is a non-constant coefficient, $\alpha(\mathbf{q}) \geq 0$, times a constant positive definite matrix, \mathcal{C} , $\mathcal{B}_a = \alpha(\mathbf{q})\mathcal{C}$: the filtered flux is,

$$\overset{\leftrightarrow}{\mathbf{F}}_a = \sqrt{\frac{\alpha}{\mathcal{J}}} \mathcal{C} \mathcal{F} \star \left(\sqrt{\mathcal{J} \alpha} \overset{\leftrightarrow}{\mathbf{G}} \right). \quad (101)$$

For example, the physical dissipation computed with the kinetic energy variables as in Sec. 2.2.1.

2. \mathcal{B}_a is a general positive definite matrix: any positive definite matrix has a Cholesky decomposition (see [30]), $\mathcal{B}_a = \mathcal{L}^T \mathcal{D} \mathcal{L}$. Thus, we define the filtered flux as,

$$\overset{\leftrightarrow}{\mathbf{F}}_a = \frac{1}{\sqrt{\mathcal{J}}} \mathcal{L}^T \sqrt{\mathcal{D}} \mathcal{F} \star \left(\sqrt{\mathcal{J} \mathcal{D} \mathcal{L}} \overset{\leftrightarrow}{\mathbf{G}} \right), \quad (102)$$

where the square root of a diagonal matrix represents a diagonal matrix whose entries are the square roots of the original matrix. Examples of this form are the physical dissipation in thermodynamic entropy variables, Sec. 2.2.2, and the Guermond–Popov fluxes, Sec. 2.2.3.

The specific form of these fluxes is later justified by stability analysis. We conclude this section by filtering the artificial viscosity flux in the volume and surface quadratures of the DG scheme (52),

$$\begin{aligned} \langle \mathcal{J} \mathbf{Q}_t, \phi \rangle_{\mathbf{E}, N} + \int_{\partial e, N} \phi^T \left(\overset{\leftrightarrow}{\mathbf{F}}_e^* - \overset{\leftrightarrow}{\mathbf{F}}_e \right) \cdot \vec{n} \, dS + \left\langle \mathbb{D} \left(\overset{\leftrightarrow}{\mathbf{F}}_e^\# \right), \phi \right\rangle_{\mathbf{E}, N} \\ = \int_{\partial e, N} \phi^T \left(\overset{\leftrightarrow}{\mathbf{F}}_v^* + \overset{\leftrightarrow}{\mathbf{F}}_a^{\mathcal{F},*} \right) \cdot \vec{n} \, dS - \left\langle \overset{\leftrightarrow}{\mathbf{F}}_v + \overset{\leftrightarrow}{\mathbf{F}}_a^{\mathcal{F}}, \vec{\nabla}_\xi \phi \right\rangle_{\mathbf{E}, N}. \end{aligned} \quad (103)$$

5.1 Stability analysis

We study the stability of the DGSEM with filtered artificial viscosity. Since inviscid and viscous terms have already been studied in other works [33, 27], we restrict ourselves to outline the main ideas to focus on the novel form of the filtered dissipation.

First, we apply the discrete Gauss law to the gradient equation (52b), and we replace its test function by the viscous and filtered artificial viscosity fluxes $\overset{\leftrightarrow}{\boldsymbol{\varphi}} = \overset{\leftrightarrow}{\mathbf{F}}_v + \overset{\leftrightarrow}{\mathbf{F}}_a^{\mathcal{F}}$,

$$\left\langle \mathcal{J} \overset{\leftrightarrow}{\mathbf{G}}, \overset{\leftrightarrow}{\mathbf{F}}_v + \overset{\leftrightarrow}{\mathbf{F}}_a^{\mathcal{F}} \right\rangle_{\mathbf{E}, N} = \int_{\partial e, N} (\mathbf{W}^* - \mathbf{W})^T \left(\overset{\leftrightarrow}{\mathbf{F}}_v + \overset{\leftrightarrow}{\mathbf{F}}_a^{\mathcal{F}} \right) \cdot \vec{n} \, dS + \left\langle \vec{\nabla}_\xi \mathbf{W}, \overset{\leftrightarrow}{\mathbf{F}}_v + \overset{\leftrightarrow}{\mathbf{F}}_a^{\mathcal{F}} \right\rangle_{\mathbf{E}, N}. \quad (104)$$

Second, we replace the test function $\phi = \mathbf{W}$ in (103)

$$\begin{aligned} \langle \mathcal{J} \mathbf{Q}_t, \mathbf{W} \rangle_{\mathbf{E}, N} + \int_{\partial e, N} \mathbf{W}^T \left(\overset{\leftrightarrow}{\mathbf{F}}_e^* - \overset{\leftrightarrow}{\mathbf{F}}_e \right) \cdot \vec{n} \, dS + \left\langle \mathbb{D} \left(\overset{\leftrightarrow}{\mathbf{F}}_e^\# \right), \mathbf{W} \right\rangle_{\mathbf{E}, N} \\ = \int_{\partial e, N} \mathbf{W}^T \left(\overset{\leftrightarrow}{\mathbf{F}}_v^* + \overset{\leftrightarrow}{\mathbf{F}}_a^{\mathcal{F},*} \right) \cdot \vec{n} \, dS - \left\langle \overset{\leftrightarrow}{\mathbf{F}}_v + \overset{\leftrightarrow}{\mathbf{F}}_a^{\mathcal{F}}, \vec{\nabla}_\xi \mathbf{W} \right\rangle_{\mathbf{E}, N}, \end{aligned} \quad (105)$$

and we replace the viscous and artificial viscosity volume term from (104) into (105) to get a single equation,

$$\begin{aligned} & \langle \mathcal{J}\mathbf{Q}_t, \mathbf{W} \rangle_{\mathbf{E},N} + \int_{\partial e,N} \mathbf{W}^T \left(\overset{\leftrightarrow}{\mathbf{F}}_e^* - \overset{\leftrightarrow}{\mathbf{F}}_e \right) \cdot \bar{\mathbf{n}} \, dS + \left\langle \mathbb{D} \left(\overset{\leftrightarrow}{\mathbf{F}}_e^\# \right), \mathbf{W} \right\rangle_{\mathbf{E},N} \\ &= \int_{\partial e,N} \left(\mathbf{W}^T \left(\overset{\leftrightarrow}{\mathbf{F}}_v + \overset{\leftrightarrow}{\mathbf{F}}_a^{\mathcal{F},*} \right) + (\mathbf{W}^* - \mathbf{W})^T \left(\overset{\leftrightarrow}{\mathbf{F}}_v + \overset{\leftrightarrow}{\mathbf{F}}_a^{\mathcal{F}} \right) \right) \cdot \bar{\mathbf{n}} \, dS - \left\langle \mathcal{J}\overset{\leftrightarrow}{\mathbf{G}}, \overset{\leftrightarrow}{\mathbf{F}}_v + \overset{\leftrightarrow}{\mathbf{F}}_a^{\mathcal{F}} \right\rangle_{\mathbf{E},N}. \end{aligned} \quad (106)$$

We first study the volume terms. From [27, 32],

$$\begin{aligned} \langle \mathcal{J}\mathbf{Q}_t, \mathbf{W} \rangle_{\mathbf{E},N} &= \langle \mathcal{J}\mathcal{E}_t \rangle_{\mathbf{E},N}, \\ \left\langle \mathbb{D} \left(\overset{\leftrightarrow}{\mathbf{F}}_e^\# \right), \mathbf{W} \right\rangle_{\mathbf{E},N} &= \int_{\partial e,N} \bar{F}_e^\mathcal{E} \cdot \bar{\mathbf{n}} \, dS + \Theta \mathcal{W}_p, \\ \left\langle \mathcal{J}\overset{\leftrightarrow}{\mathbf{G}}, \overset{\leftrightarrow}{\mathbf{F}}_v \right\rangle_{\mathbf{E},N} &= \left\langle \mathcal{J}\overset{\leftrightarrow}{\mathbf{G}}, \mathcal{B}_v \overset{\leftrightarrow}{\mathbf{G}} \right\rangle_{\mathbf{E},N} = \langle D_v \rangle^{\mathbf{E},N} \geq 0. \end{aligned} \quad (107)$$

Therefore, we transform (106) into

$$\begin{aligned} & \langle \mathcal{J}\mathcal{E}_t \rangle_{\mathbf{E},N} + \int_{\partial e,N} \mathbf{W}^T \left(\overset{\leftrightarrow}{\mathbf{F}}_e^* - \overset{\leftrightarrow}{\mathbf{F}}_e \right) \cdot \bar{\mathbf{n}} \, dS + \int_{\partial e,N} \bar{F}_e^\mathcal{E} \cdot \bar{\mathbf{n}} \, dS + \Theta \mathcal{W}_p + \langle D_v \rangle^{\mathbf{E},N} + \left\langle \mathcal{J}\overset{\leftrightarrow}{\mathbf{G}}, \overset{\leftrightarrow}{\mathbf{F}}_a^{\mathcal{F}} \right\rangle_{\mathbf{E},N} \\ &= \int_{\partial e,N} \left(\mathbf{W}^T \left(\overset{\leftrightarrow}{\mathbf{F}}_v + \overset{\leftrightarrow}{\mathbf{F}}_a^{\mathcal{F},*} \right) + (\mathbf{W}^* - \mathbf{W})^T \left(\overset{\leftrightarrow}{\mathbf{F}}_v + \overset{\leftrightarrow}{\mathbf{F}}_a^{\mathcal{F}} \right) \right) \cdot \bar{\mathbf{n}} \, dS. \end{aligned} \quad (108)$$

We now study the stability of the volume term associated to the filtered artificial viscosity. We study the two options provided in Sec. 5.

1. The non-constant coefficient times a constant positive definite matrix (101)

$$\langle D_a \rangle^{\mathbf{E},N} = \left\langle \mathcal{J}\overset{\leftrightarrow}{\mathbf{G}}, \sqrt{\frac{\alpha}{\mathcal{J}}} \mathcal{C}\mathcal{F}^* \left(\sqrt{\mathcal{J}\alpha} \overset{\leftrightarrow}{\mathbf{G}} \right) \right\rangle_{\mathbf{E},N} = \left\langle \sqrt{\mathcal{J}\alpha} \overset{\leftrightarrow}{\mathbf{G}}, \mathcal{C}\mathcal{F}^* \left(\sqrt{\mathcal{J}\alpha} \overset{\leftrightarrow}{\mathbf{G}} \right) \right\rangle_{\mathbf{E},N} \geq 0. \quad (109)$$

2. The general positive definite matrix (102)

$$\langle D_a \rangle^{\mathbf{E},N} = \left\langle \mathcal{J}\overset{\leftrightarrow}{\mathbf{G}}, \frac{1}{\sqrt{\mathcal{J}}} \mathcal{L}^T \sqrt{\mathcal{D}} \mathcal{F}^* \left(\sqrt{\mathcal{J}\mathcal{D}} \overset{\leftrightarrow}{\mathbf{G}} \right) \right\rangle_{\mathbf{E},N} = \left\langle \sqrt{\mathcal{J}\mathcal{D}} \overset{\leftrightarrow}{\mathbf{G}}, \mathcal{F}^* \left(\sqrt{\mathcal{J}\mathcal{D}} \overset{\leftrightarrow}{\mathbf{G}} \right) \right\rangle_{\mathbf{E},N} \geq 0. \quad (110)$$

Where we used Property 4 to conclude that the two possibilities introduce volume dissipative terms. A similar conclusion was reached by Lundquist and Nordström in [50], where they defined the filter kernel as $\mathcal{J}^{-1/2} \mathcal{F} \mathcal{J}^{1/2}$ to ensure the so called *time-stability*. Therefore, we can write,

$$\begin{aligned} & \langle \mathcal{J}\mathcal{E}_t \rangle_{\mathbf{E},N} + \int_{\partial e,N} \mathbf{W}^T \left(\overset{\leftrightarrow}{\mathbf{F}}_e^* - \overset{\leftrightarrow}{\mathbf{F}}_e \right) \cdot \bar{\mathbf{n}} \, dS + \int_{\partial e,N} \bar{F}_e^\mathcal{E} \cdot \bar{\mathbf{n}} \, dS + \Theta \mathcal{W}_p + \langle D_v \rangle^{\mathbf{E},N} + \langle D_a \rangle^{\mathbf{E},N} \\ &= \int_{\partial e,N} \left(\mathbf{W}^T \left(\overset{\leftrightarrow}{\mathbf{F}}_v + \overset{\leftrightarrow}{\mathbf{F}}_a^{\mathcal{F},*} \right) + (\mathbf{W}^* - \mathbf{W})^T \left(\overset{\leftrightarrow}{\mathbf{F}}_v + \overset{\leftrightarrow}{\mathbf{F}}_a^{\mathcal{F}} \right) \right) \cdot \bar{\mathbf{n}} \, dS. \end{aligned} \quad (111)$$

With the volume terms addressed, we study the boundary terms. To do this, we sum (111) over all the mesh elements,

$$\langle \mathcal{E}_t \rangle^N + \text{IBT} + \text{PBT} + \sum_e \langle D_v \rangle^{E,N} + \sum_e \langle D_a \rangle^{E,N} + \theta \sum_e \mathcal{W}_p = 0, \quad (112)$$

where $\langle \mathcal{E}_t \rangle^N = \sum_e \langle \mathcal{J} \mathcal{E}_t \rangle_{E,N}$ is the total entropy derivative, IBT are the interior boundary terms,

$$\begin{aligned} \text{IBT} = \text{IBT}_e + \text{IBT}_v + \text{IBT}_a = & - \sum_{\substack{\text{interior} \\ \text{faces}}} \int_{f,N} \left(\left[\bar{F}_e^\mathcal{E} \right] + \left[\mathbf{W} \right]^T \bar{\mathbf{F}}_e^{\leftrightarrow \star} - \left[\mathbf{W}^T \bar{\mathbf{F}}_e \right] \right) \cdot \bar{\mathbf{n}}_L \, dS \\ & + \sum_{\substack{\text{interior} \\ \text{faces}}} \int_{f,N} \left(\left[\mathbf{W} \right]^T \bar{\mathbf{F}}_v^{\leftrightarrow \star} + \mathbf{W}^{\star,T} \left[\bar{\mathbf{F}}_v \right] - \left[\mathbf{W}^T \bar{\mathbf{F}}_v \right] \right) \cdot \bar{\mathbf{n}}_L \, dS \\ & + \sum_{\substack{\text{interior} \\ \text{faces}}} \int_{f,N} \left(\left[\mathbf{W} \right]^T \bar{\mathbf{F}}_a^{\leftrightarrow \mathcal{F},\star} + \mathbf{W}^{\star,T} \left[\bar{\mathbf{F}}_a \right] - \left[\mathbf{W}^T \bar{\mathbf{F}}_a \right] \right) \cdot \bar{\mathbf{n}}_L \, dS, \end{aligned} \quad (113)$$

and PBT are the physical boundary terms,

$$\begin{aligned} \text{PBT} = \text{PBT}_e + \text{PBT}_v + \text{PBT}_a = & \sum_{\substack{\text{boundary} \\ \text{faces}}} \int_{f,N} \left(\bar{F}_e^\mathcal{E} + \mathbf{W}^T \bar{\mathbf{F}}_e^{\leftrightarrow \star} - \mathbf{W}^T \bar{\mathbf{F}}_e \right) \cdot \bar{\mathbf{n}} \, dS \\ & - \sum_{\substack{\text{boundary} \\ \text{faces}}} \int_{f,N} \left(\mathbf{W}^T \bar{\mathbf{F}}_v^{\leftrightarrow \star} + \mathbf{W}^{\star,T} \bar{\mathbf{F}}_v - \mathbf{W}^T \bar{\mathbf{F}}_v \right) \cdot \bar{\mathbf{n}} \, dS \\ & - \sum_{\substack{\text{boundary} \\ \text{faces}}} \int_{f,N} \left(\mathbf{W}^T \bar{\mathbf{F}}_a^{\leftrightarrow \mathcal{F},\star} + \mathbf{W}^{\star,T} \bar{\mathbf{F}}_a - \mathbf{W}^T \bar{\mathbf{F}}_a \right) \cdot \bar{\mathbf{n}} \, dS. \end{aligned} \quad (114)$$

The interior boundary terms for the inviscid and viscous terms have been studied in [33, 27]. If one uses the two-point entropy conserving flux as the numerical flux, $\text{IBT}_e = 0$, whereas for the dissipative flux, $\text{IBT}_e \geq 0$. For viscous fluxes, the BR1 scheme gives $\text{IBT}_v = 0$. We have also used the BR1 scheme for the artificial dissipative fluxes, and therefore we also get $\text{IBT}_a = 0$,

$$\left[\mathbf{W} \right]^T \bar{\mathbf{F}}_a^{\leftrightarrow \mathcal{F},\star} + \mathbf{W}^{\star,T} \left[\bar{\mathbf{F}}_a \right] - \left[\mathbf{W}^T \bar{\mathbf{F}}_a \right] = \left[\mathbf{W} \right]^T \{ \{ \bar{\mathbf{F}}_a \} \} + \{ \{ \mathbf{W} \} \}^T \left[\bar{\mathbf{F}}_a \right] - \left[\mathbf{W}^T \bar{\mathbf{F}}_a \right] = 0. \quad (115)$$

Similarly, the physical boundary terms for the inviscid and viscous terms were studied in [51] for the wall boundary condition. This analysis concluded that $\text{PBT}_e = 0$ if one simply imposes the boundary data, and $\text{PBT}_e \geq 0$ if one uses the dissipative numerical flux with a ghost state. In the case of the viscous fluxes, $\text{PBT}_v = 0$, and for the artificial viscosity fluxes, the physical boundary terms are also zero. For the no-slip wall,

$$\mathbf{W}^T \bar{\mathbf{F}}_a^{\leftrightarrow \mathcal{F},\star} + (\mathbf{W}^\star - \mathbf{W})^T \bar{\mathbf{F}}_a^{\leftrightarrow \mathcal{F}} = \mathbf{W}^T (0, F_{a,2}, F_{a,3}, F_{a,4}, 0) + (0, -W_2, -W_3, -W_4, 0)^T \bar{\mathbf{F}}_a^{\leftrightarrow \mathcal{F}} = 0, \quad (116)$$

and for the free-slip wall,

$$\mathbf{W}^T \bar{\mathbf{F}}_a^{\leftrightarrow \mathcal{F},\star} + (\mathbf{W}^\star - \mathbf{W})^T \bar{\mathbf{F}}_a^{\leftrightarrow \mathcal{F}} = (\mathbf{W} - \mathbf{W})^T \bar{\mathbf{F}}_a^{\leftrightarrow \mathcal{F}} = 0. \quad (117)$$

We conclude the stability analysis as we confirm that the thermodynamic entropy is monotonic and decreases due to the numerical dissipation of the inviscid numerical flux at the inter–element and physical faces, and the artificial and physical dissipation at the interior of the elements,

$$\langle \mathcal{E}_t \rangle^N + \Theta \sum_e \mathcal{W}_p = -\text{IBT}_e - \text{PBT}_e - \sum_e \langle D_v \rangle^{\text{E},N} - \sum_e \langle D_a \rangle^{\text{E},N} \leq 0. \quad (118)$$

Regarding the kinetic energy, the work introduced by the pressure gradient cannot be bounded. However, although the kinetic energy is not a mathematical entropy in the strict sense, schemes based on kinetic energy preservation [31] represent a popular choice for subsonic flows, given that the resulting schemes are still robust and have a lower computational cost than those based on the thermodynamic entropy (which are the preferred option to solve supersonic flows, where oscillations in the energy equation become important).

In any case, we are able to adjust the artificial dissipation $D_a^{\text{E},N}$ with the selection of the artificial viscosities, and the filter kernel \mathcal{F} .

5.2 Linear von Neumann analysis

Before continuing with the numerical experiments, as in other works [22, 52, 24, 53, 54], we perform a von Neumann analysis to characterise the SVV in the one–dimensional advection–diffusion equation with constant coefficients. This will allow us to better understand the dissipative behaviour of the SVV filtering technique at different scales, knowledge that we can use to understand the results we find in the posterior Navier–Stokes experiments in Sec. 6. Starting from the continuous formulation,

$$u_t + au_x = \mu u_{xx}, \quad (119)$$

where $a > 0$ is the advection velocity and $\mu > 0$, the viscosity, we introduce a wave-like solution $u(x, t) = e^{i(kx - \omega t)} = u_0(x)e^{-i\omega t}$, to determine the dispersion relation, $\omega(k)$, which shows the behavior of a monochromatic wave when traversing the domain of interest. In this case,

$$-i\omega + iak = -\mu k^2, \quad \omega = ak - i\mu k^2, \quad (120)$$

implying that $u(x, t) = e^{-\mu k^2 t} e^{ik(x - at)}$ and thus, the wave velocity is a and the dissipation is μk^2 . The discretization of (119) induces errors into the solution that lead to a modified dispersion relation. If $\Re(\omega) \neq ak$, the numerical scheme is introducing a dispersion error that makes the waves to move at velocities different from the exact one and, if this velocity depends on k , the different components of non–monochromatic waves will drift, deforming it as it traverses the domain. The imaginary part of ω is directly related to the dissipation of the scheme and thus, a negative value means that the scheme is stable.

In this von Neumann analysis of the DGSEM with SVV dissipation we use a simple upwinding Riemann solver for the advective term, and we keep the BR1 scheme for the viscous part,

$$aU^* = a\{\{U\}\} - \frac{|a|}{2} \llbracket U \rrbracket, \quad \mu G^* = \{\{\mu G\}\}, \quad U^* = \{\{U\}\}, \quad (121)$$

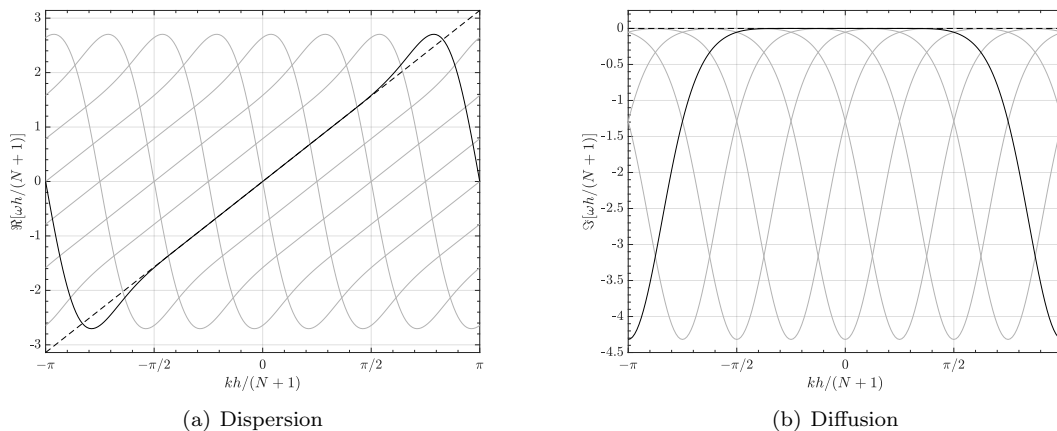


Fig. 2 Dispersion–diffusion curves of the DGSEM discretization of (119) with $N = 7$ and no viscosity. Dashed lines represent the expected result from the continuous equation.

where, as we have previously done, for instance, in (39), we define the gradient of the solution as $G = U_x$. The dispersion–dissipation errors with no viscosity and $N = 7$ have been represented in Fig. 2 to serve as a starting point.

The SVV is introduced in (119) by redefining the viscous term as,

$$\mu G = \mu_a \mathcal{H} G, \quad \mathcal{H} = B \hat{\mathcal{F}} F, \quad \hat{\mathcal{F}}_i = \text{diag} \left[\left(\frac{i}{N} \right)^{P_{\text{SVV}}} \right], \quad (122)$$

where the matrix \mathcal{H} applies the filter kernel defined by Moura et al. [22], $\hat{\mathcal{F}}$, to the gradients, G , as we showed in Sec. 4.1. In this formulation, the artificial viscosity is controlled with two parameters: μ_a and P_{SVV} , and we can now compute the curve $\omega(k)$ as shown in Fig. 3 for a constant value of $\mu_a = 0.01$. We want to note that this choice of filter kernel allows us to recover the original viscous operator by selecting $P_{\text{SVV}} = 0$ and thus, $\mathcal{H} = \mathcal{I}$, but the only way to completely eliminate the viscosity is by setting $\mu_a = 0$.

The results are presented in Fig. 3 and are in agreement with those in [24]. As we expected, the effect of P_{SVV} is more evident for low frequency waves, where the SVV is responsible for almost all the dissipation in this region. For the rest of wavenumbers, the addition of viscosity evidently increases dissipation and, even if it can be controlled with the filter kernel to some point, it is comparatively smaller than the one already added by the Riemann solver. These results are also in line with our purpose, since we can still dissipate unwanted oscillations in regions with discontinuities while keeping smoother regions almost unaffected.

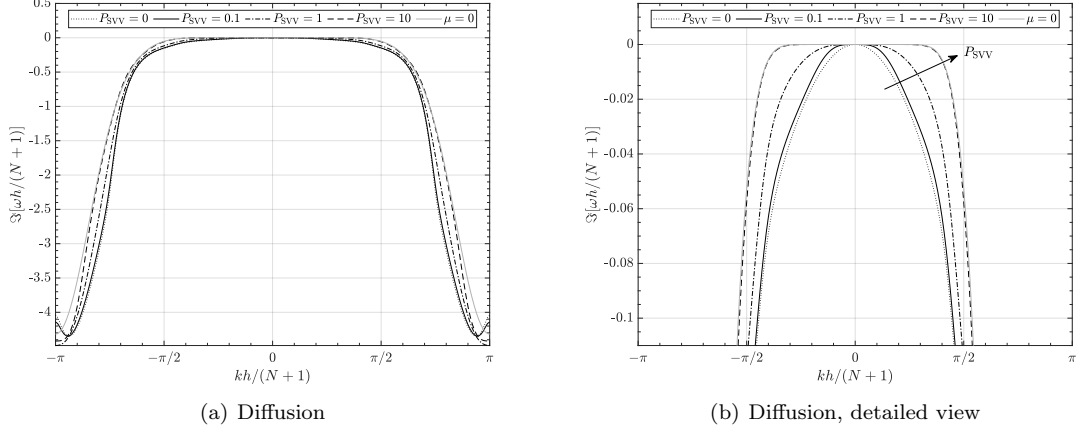


Fig. 3 Dispersion–diffusion curves with $\mu_a = 0.01$, $N = 7$ and different values of P_{SVV} .

6 Numerical experiments

In this section we present numerical experiments where the benefits of the filtered artificial viscosity are compared against the non-filtered DGSEM and other reference solutions from the literature. We apply the filter kernel, taken from [22], in all the cases,

$$\hat{\mathcal{F}}_i^{1D} = \left(\frac{i}{N} \right)^{P_{SVV}}. \quad (123)$$

6.1 Taylor–Green vortex

We repeat the experiment of [24] with the entropy stable version of the SVV. The Taylor–Green vortex case is initialized with a periodic flow field representing a set of vortices that evolve in time, transferring their energy to lower scales, where it is finally dissipated. Thus, it is a good test for analyzing the dissipative features of our numerical scheme, including the SVV. In our simulations, the computational domain is a periodic $[0, 2\pi]^3$ cube divided into 8^3 elements with approximation degree $N = 8$, and the initial condition is

$$\begin{aligned} \rho &= 1, \\ u &= \sin(x) \cos(y) \cos(z), \\ v &= -\cos(x) \sin(y) \cos(z), \\ w &= 0, \\ p &= 100 + \frac{1}{16} [\cos(2x) \cos(2z) + 2 \cos(2y) + 2 \cos(2x) + \cos(2y) \cos(2z)] \end{aligned} \quad (124)$$

We aim to prove that the addition of the filtered artificial viscosity in the DGSEM does not destabilize the energy preserving properties of the scheme, so we discretize the inviscid term with

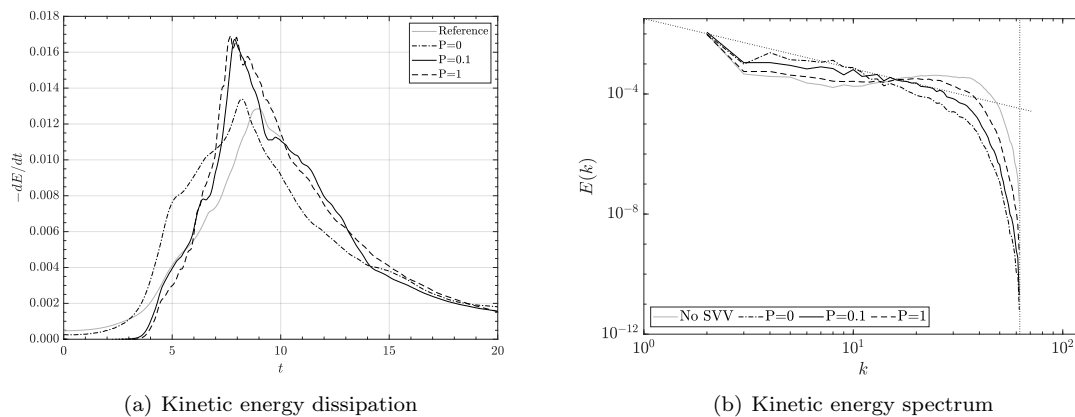


Fig. 4 Kinetic energy dissipation and spectrum of the inviscid Taylor–Green case at $t = 20$ with a 8^3 elements cartesian grid and $N = 8$. The LES viscosity is excessively dissipative and the SVV can control it, having an optimum value $P_{\text{SVV}} \approx 0.1$. Reference data obtained from [56] with a resolution of 768^3 .

the kinetic energy preserving split–form from Pirozzoli [41] and use a low dissipation Roe, Riemann solver [7] to add dissipation in the region of higher wavenumbers.

We apply a high–pass filtered Navier–Stokes viscosity to additionally increase dissipation in lower/medium scales, controlling it through P_{SVV} . Regarding the viscosity, we compute its value at runtime from a LES (Smagorinsky) formulation,

$$\mu_a = C_S^2 \Delta^2 |S|, \quad \Delta^3 = \frac{\text{Cell volume}}{(N+1)^3}, \quad S_{ij} = \frac{1}{2} \left(\frac{\partial u_i}{\partial x_j} + \frac{\partial u_j}{\partial x_i} \right), \quad (125)$$

with $C_S = 0.2$. In this way, we eliminate one parameter and, at the same time, we also exploit the benefits of this LES approach to resolve turbulence. Similarly as we did in von Neumann analysis of the one–dimensional advection–diffusion, we want to find the effect of the artificial viscosity in different scales. To do so, we acknowledge that the theoretical kinetic energy spectrum of the TGV obeys the law $E(k) \propto k^{-5/3}$ [55], thus decaying for higher wavenumbers. Due to the previously mentioned lack of numerical dissipation of the DGSEM and the use of Pirozzoli’s split–form, an accumulation of kinetic energy is expected for high wavenumbers, where the Riemann solver and the SVV replace the dissipation that takes place in well resolved cases.

A representation of the evolution of the kinetic energy, E , and its spectrum for different values of P_{SVV} at $t = 20$ (see Fig. 4) shows that the LES model ($P_{\text{SVV}} = 0$) introduces excessive dissipation. This represents the perfect use case for the methodology presented, as we aim to control this excess by adjusting the filter kernel coefficient. In agreement with the results from von Neumann analysis, the SVV does not change significantly the behaviour of the higher frequency modes, concentrating its effect in the low to medium wavenumbers. As we expected, the introduction of viscosity in these regions helps to dissipate energy in all the scales and not only in the smallest ones, avoiding its accumulation in high–frequency modes and flattening the energy spectrum. For an optimum that we find to be $P_{\text{SVV}} \approx 0.1$, it closely resembles that of the $k^{-5/3}$ theoretical law in most parts of the range

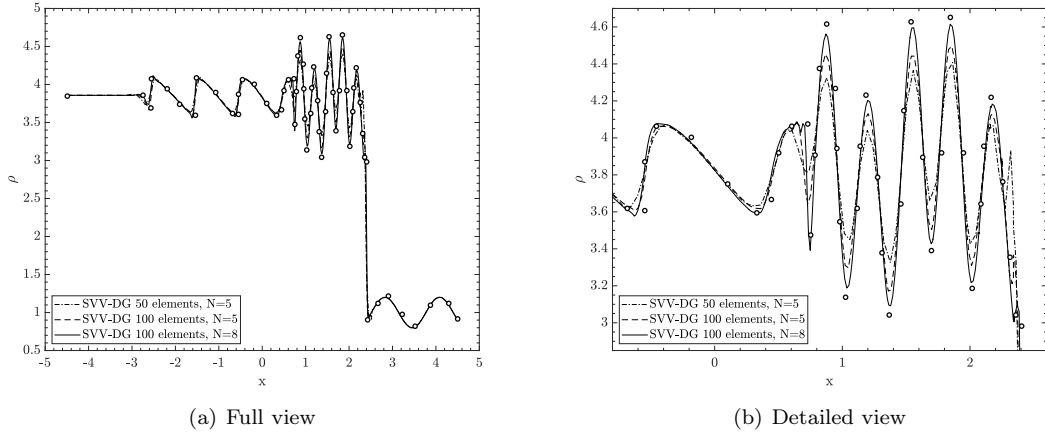


Fig. 5 Density solution of the one–dimensional Shu–Osher problem. The solid lines represent the DG solution with the SVV dissipation developed in this work, and the dots represent the reference solution of [57] using an ENO–RF–S–3 scheme with 1600 degrees of freedom.

of wavenumbers resolved by the scheme. This can also be seen in Fig. 4(a), where we compare the energy dissipation of our scheme with a reference solution from Rees et al. [56] at $Re = 1600$. During the first five seconds, the flow is essentially laminar and our scheme adds less dissipation than the reference. After that, higher-frequency modes gain importance and the dissipation rate increases to a similar extent of that of the reference to prevent energy accumulation in the smaller scales.

6.2 Shock capturing: Shu–Osher problem

The one–dimensional Shu–Osher problem describes the evolution of a shock wave that swallows a density fluctuation as it advances. Since the solution combines a strong shock with smooth oscillations, this benchmark is useful to assess how the dissipation is able to both, control the shock and vanish in non–shocky regions at the same time.

The computational domain is $x \in [-4.5, 4.5]$, and the initial condition is

$$(\rho, u, p) = \begin{cases} (3.857143, 2.629369, 10.3333) & \text{if } x \leq -4, \\ (1 + 0.2 \sin 5x, 0, 1) & \text{if } x > -4. \end{cases} \quad (126)$$

To ensure that the solution is physically meaningful, here we use an entropy stable formulation, discretizing the inviscid term with Chandrashekar’s split–form [42] and the matrix dissipation Riemann solver (56), and adding SVV filtered Guermond–Popov fluxes with thermodynamic entropy variables. We have found that the SVV filtering is not enough to control the oscillations near the strong shock, and we have implemented a simple sensor, s_1 , based on the density gradient to set $P_{SVV} = 0$ in the

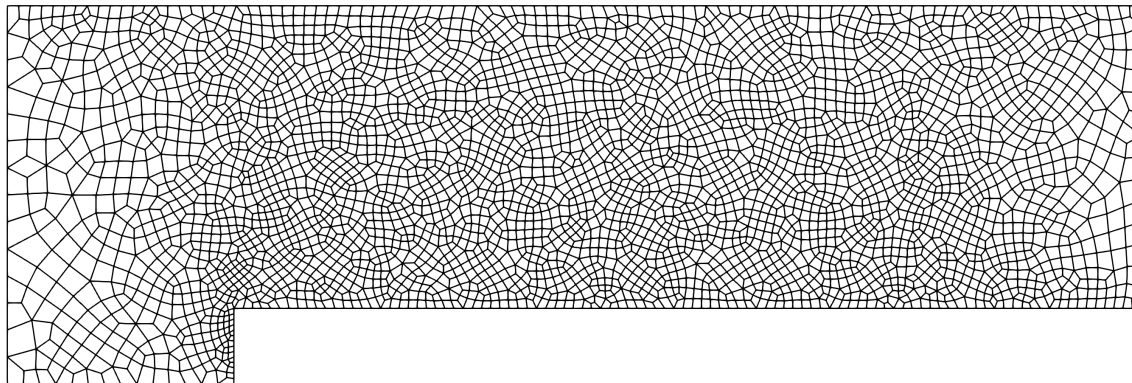


Fig. 6 Mesh for the forward facing step case with 3653 elements.

discontinuity ($s_1 > 10$) and $P_{\text{SVV}} = 2$ elsewhere,

$$s_1 = \sqrt{\sum_{i=0}^N w_i \left(\frac{\partial \rho}{\partial x} \right)_i^2}. \quad (127)$$

The results are shown in Fig. 5, where we have tested this approach with two different meshes and approximation orders. The coarsest mesh contains 50, 5th order elements, while the finest one has 100 elements with approximation orders $N = 5$ and $N = 8$, leading to 300, 600 and 900 solution nodes for each one of the three test cases, respectively. As expected, an increasing number of nodes returns a better approximation to the reference solution (see [57]); however, all the cases show a similar behaviour, reproducing all the features of the flow. The main shock is well resolved due to the effect of the sensor. The density regularization of the Guermond–Popov fluxes removes further fluctuations in the lower region of the shock, and the introduction of the SVV filtering is responsible for the smoothing of the solution in the downstream of the strong shock. This is very successful at eliminating most of the spurious oscillations while it leaves the lower order modes, corresponding to the flow features, almost unaltered.

6.3 Shock capturing: Mach 3 forward facing step

Finally, we solve the flow over a forward facing step at Mach 3 with a very coarse mesh to put to test the capabilities of the SVV shock capturing scheme. The mesh contains 3653 quadrilateral elements with approximation order $N = 7$ and, to make the case more challenging, there is no intentional alignment between the element interfaces and the flow structure. Since we are interested in properly capturing the strong shocks that appear before the step, we keep using the entropy stable scheme and use the two–point flux from Chandrashekar [42] with matrix dissipation (56) for the inter–element fluxes, and the Guermond–Popov filtered viscous fluxes for the artificial viscosity term.

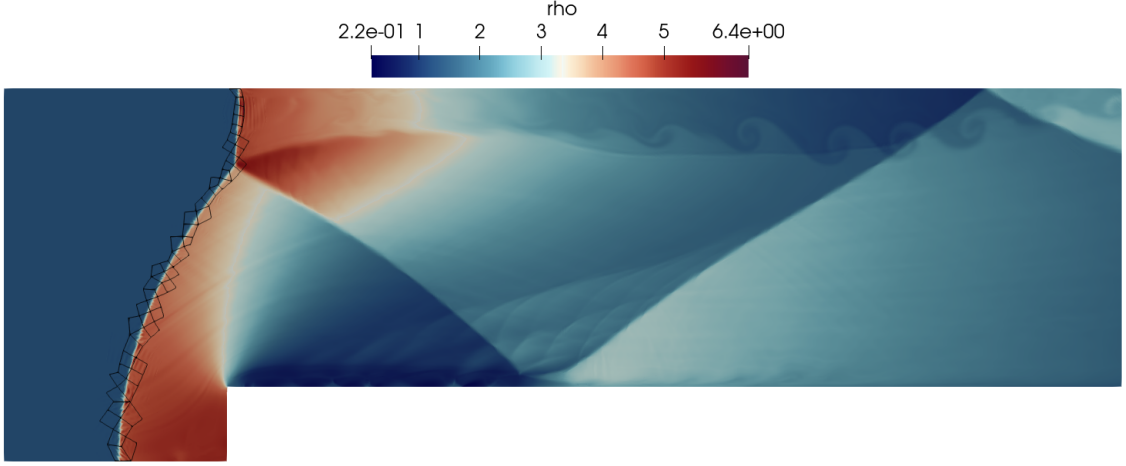


Fig. 7 Density contour of the two-dimensional forward facing step at $t = 10$.

As we did in the previous section, we detect the discontinuities with the sensor s_2 , defined as an extension of (127) to two dimensions,

$$s_2 = \sqrt{\sum_{i,j=0}^N w_i w_j \left(\vec{\nabla} \rho \right)_{ij}^2}, \quad (128)$$

and set $\mu_1 = \mu_2 = \alpha_1 = 0.0005$ and $\alpha_2 = 0$ according to

- $s_1 < 1$: $P_{\text{SVV}} = 4$, $\mu_\alpha = \mu_1$ and $\alpha_\alpha = \alpha_1$,
- $s_1 \geq 1$: $P_{\text{SVV}} = 0$, $\mu_\alpha = \mu_2$ and $\alpha_\alpha = \alpha_2$.

We use a short run (until $t = 1$) with higher viscosity ($\mu_1 = \mu_2 = \alpha_1 = 0.001$ and $\alpha_2 = 0$) to start the case with the entropy stable SVV, and represent the solution at $t = 10$ in Fig. 7. The thickness of the main shock is well resolved within the size of one element and, at the same time, the smoother features of the flow, such as the turbulent wakes that start at the mixing layer of the top or the corner of the step, are also captured.

7 Conclusions

In this work we have proposed an entropy stable SVV filtered artificial viscosity for the DGSEM that is able to tackle some of the usual drawbacks of the discontinuous Galerkin methods. The revision of the classical SVV filtering technique has allowed us to prove its entropy stability after small modifications. As it is usual in SVV methods, the intensity of the dissipation is controlled through a modulated viscosity coefficient, whereas its wavenumber profile is specified by the filter kernel. Moreover, we also include an entropy stable discretization of the Guermond–Popov fluxes [19] using the Bassi–Rebay 1 scheme. These fluxes have been filtered with the SVV technique and applied to solve usual shock

capturing benchmark problems. Having accounted for this properties, we have tested its capabilities regarding two different mathematical entropy functions: the kinetic energy (used in subsonic flows) and the thermodynamical entropy (used in supersonic flows).

For the kinetic energy, we have used a turbulent case and we have shown that a specific choice of the parameters reproduces the expected energy decay for the scales resolved by the DGSEM. Additionally, we have also found that this approach can be easily coupled with other schemes to provide better results. Specifically, as in [24], we implement an SVV-LES method that automates the computation of the viscosity and improves the results for a wide range of values of the SVV exponent, reducing the impact of the choice of P_{SVV} on the solution. However, in contrast to the method presented in [24], the approach described herein is entropy stable.

For the thermodynamic entropy, we have simulated the well known Shu–Osher one–dimensional case and a supersonic two–dimensional forward facing step, where the SVV approach based on the Guermond–Popov fluxes [19] has proven to capture strong shocks fully contained within a single element and, at the same time, resolve detailed features of the flow in smoother regions.

8 Acknowledgments

Andrés Mateo has received funding from the Universidad Politécnica de Madrid under the Programa Propio PhD programme. Eusebio Valero acknowledge the funding received from the European Commission through the Global Fellowship Grant FLOWCID (Grant Agreement-101019137), and from the Ministerio de Ciencia, Innovación y Universidades of Spain under the project SIMOPAIR (Ref: RTI2018-480 097075-B-I00).

A Effect of the filter kernel parameter

The entropy–stable SVV approach developed in this work adds a new parameter, P_{SVV} , controlling the shape of the filter kernel, \mathcal{F} . However, there is no specific strategy to set its value, and a set of cases must be run to find it. Our simulations indicate that values of $O(1)$ are appropriate for supersonic flows, while turbulent cases need a more flat dissipation profile, with $P_{\text{SVV}} \approx O(10^{-2})$ even without the help of the LES approach.

We show in this Appendix (Figure 8) some one–dimensional test cases performed with different values of P_{SVV} . Although we have chosen the Shu–osher problem in this section, the effect of the shape parameter is similar in other cases and dimensions.

It is easily seen from Figure 8 that there is only a range of values for which the solution remains close to the reference, quickly degrading when P_{SVV} is out it. This loss of accuracy is observed from the first time iterations, being more evident if discontinuities are present. This makes the trial and error process of finding a “good” value for P_{SVV} somewhat qualitative, but also not especially expensive.

B Navier–Stokes viscous flux with kinetic energy variables

Kinetic energy stability constitutes a particular case of stability but, since the last entropy variable (23) is zero, the energy equation is never involved in the stability analysis. Because of that, we have not included the dissipative terms

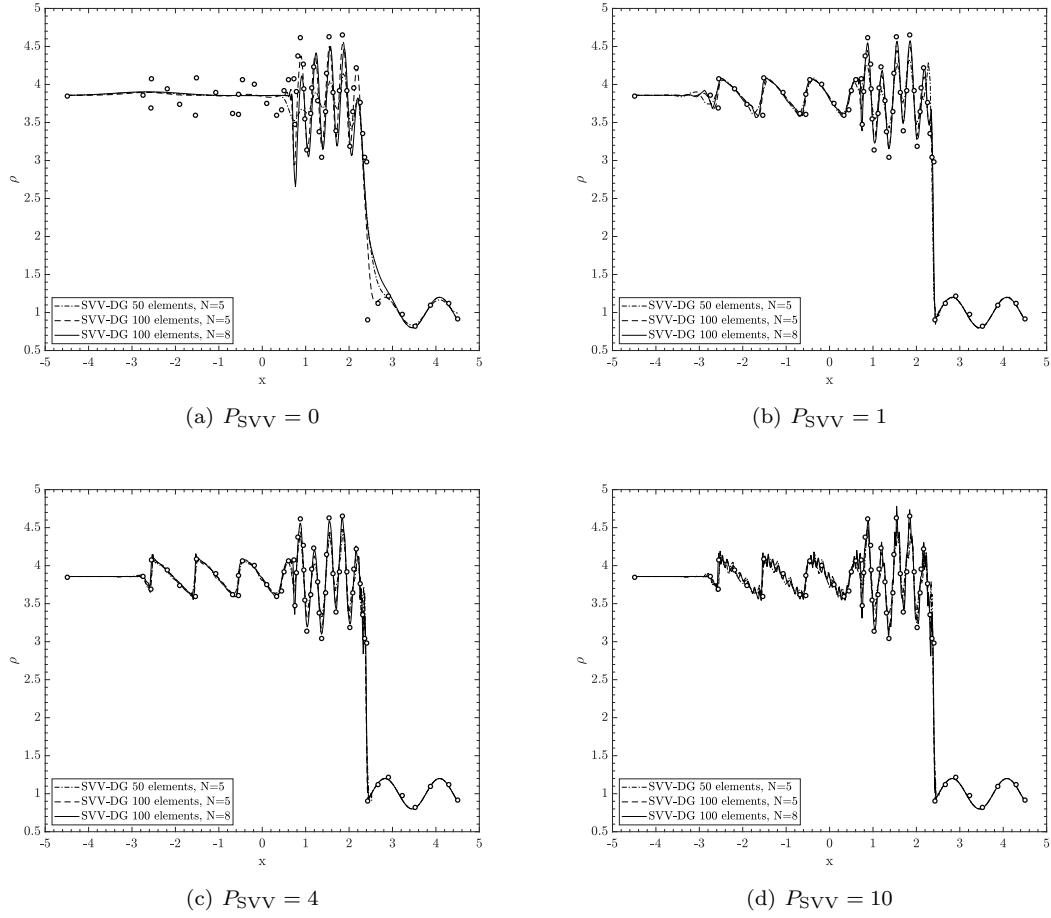


Fig. 8 Density solution of the one-dimensional Shu–Osher problem with different filter kernel shapes. The solid lines represent the DG solution with the SVV dissipation developed in this work, and the dots represent the reference solution of [57] using an ENO-RF-S-3 scheme with 1600 degrees of freedom.

of the energy equation into matrix $\mathcal{B}_v^{\mathcal{K}}$, but we add them separately to the viscous fluxes,

$$\overleftrightarrow{\mathbf{f}}_v = \mu \mathcal{C}_v^{\mathcal{K}} \overleftrightarrow{\nabla} \mathbf{w}^{\mathcal{K}} + (\boldsymbol{\tau} \cdot \bar{\mathbf{u}} + \bar{q}) \mathbf{e}_5, \quad (129)$$

with $\underline{C}_{v,ij}^{\mathcal{K}} = \underline{C}_{v,ji}^{\mathcal{K},T}$ and,

$$\begin{aligned} \underline{C}_{v,11}^{\mathcal{K}} &= \begin{pmatrix} 0 & 0 & 0 & 0 & 0 \\ 0 & \frac{4}{3} & 0 & 0 & 0 \\ 0 & 0 & 1 & 0 & 0 \\ 0 & 0 & 0 & 1 & 0 \\ 0 & 0 & 0 & 0 & 0 \end{pmatrix}, \quad \underline{C}_{v,22}^{\mathcal{K}} = \begin{pmatrix} 0 & 0 & 0 & 0 & 0 \\ 0 & 1 & 0 & 0 & 0 \\ 0 & 0 & \frac{4}{3} & 0 & 0 \\ 0 & 0 & 0 & 1 & 0 \\ 0 & 0 & 0 & 0 & 0 \end{pmatrix}, \quad \underline{C}_{v,33}^{\mathcal{K}} = \begin{pmatrix} 0 & 0 & 0 & 0 & 0 \\ 0 & 1 & 0 & 0 & 0 \\ 0 & 0 & 1 & 0 & 0 \\ 0 & 0 & 0 & \frac{4}{3} & 0 \\ 0 & 0 & 0 & 0 & 0 \end{pmatrix}, \\ \underline{C}_{v,12}^{\mathcal{K}} &= \begin{pmatrix} 0 & 0 & 0 & 0 & 0 \\ 0 & 0 & -\frac{2}{3} & 0 & 0 \\ 0 & 1 & 0 & 0 & 0 \\ 0 & 0 & 0 & 0 & 0 \\ 0 & 0 & 0 & 0 & 0 \end{pmatrix}, \quad \underline{C}_{v,13}^{\mathcal{K}} = \begin{pmatrix} 0 & 0 & 0 & 0 & 0 \\ 0 & 0 & 0 & -\frac{2}{3} & 0 \\ 0 & 0 & 0 & 0 & 0 \\ 0 & 1 & 0 & 0 & 0 \\ 0 & 0 & 0 & 0 & 0 \end{pmatrix}, \quad \underline{C}_{v,23}^{\mathcal{K}} = \begin{pmatrix} 0 & 0 & 0 & 0 & 0 \\ 0 & 0 & 0 & 0 & 0 \\ 0 & 0 & 0 & -\frac{2}{3} & 0 \\ 0 & 0 & 1 & 0 & 0 \\ 0 & 0 & 0 & 0 & 0 \end{pmatrix}, \end{aligned} \quad (130)$$

such that $\underline{C}_v^{\mathcal{K}}$ is positive definite.

C Navier–Stokes viscous flux with thermodynamic entropy variables

The viscous flux with thermodynamic entropy variables is expressed in terms of a non-linear block matrix,

$$\overleftrightarrow{\mathbf{f}}_v = \frac{\mu p}{\rho} \tilde{\mathbf{B}}_v^{\mathcal{S}} \vec{\nabla} \mathbf{w}^{\mathcal{S}}, \quad (131)$$

where the matrix $\tilde{\mathbf{B}}_v^{\mathcal{S}}$ is defined as,

$$\begin{aligned} \tilde{\underline{B}}_{v,11}^{\mathcal{S}} &= \begin{pmatrix} 0 & 0 & 0 & 0 & 0 \\ 0 & \frac{4}{3} & 0 & 0 & \frac{4}{3}u \\ 0 & 0 & 1 & 0 & v \\ 0 & 0 & 0 & 1 & w \\ 0 & \frac{4}{3}u & v & w & \frac{1}{3}u^2 + v_{\text{tot}}^2 + \frac{\theta p}{\rho} \end{pmatrix}, \quad \tilde{\underline{B}}_{v,22}^{\mathcal{S}} = \begin{pmatrix} 0 & 0 & 0 & 0 & 0 \\ 0 & 1 & 0 & 0 & u \\ 0 & 0 & \frac{4}{3} & 0 & \frac{4}{3}v \\ 0 & 0 & 0 & 1 & w \\ 0 & u & \frac{4}{3}v & w & \frac{1}{3}v^2 + v_{\text{tot}}^2 + \frac{\theta p}{\rho} \end{pmatrix}, \\ \tilde{\underline{B}}_{v,33}^{\mathcal{S}} &= \begin{pmatrix} 0 & 0 & 0 & 0 & 0 \\ 0 & 1 & 0 & 0 & u \\ 0 & 0 & 1 & 0 & v \\ 0 & 0 & 0 & \frac{4}{3} & \frac{4}{3}w \\ 0 & u & v & \frac{4}{3}w & \frac{1}{3}w^2 + v_{\text{tot}}^2 + \frac{\theta p}{\rho} \end{pmatrix}, \quad \tilde{\underline{B}}_{v,12}^{\mathcal{S}} = \begin{pmatrix} 0 & 0 & 0 & 0 & 0 \\ 0 & 0 & -\frac{2}{3} & 0 & -\frac{2}{3}v \\ 0 & 1 & 0 & 0 & u \\ 0 & 0 & 0 & 0 & 0 \\ 0 & v & -\frac{2}{3}u & 0 & \frac{1}{3}uv \end{pmatrix}, \\ \tilde{\underline{B}}_{v,13}^{\mathcal{S}} &= \begin{pmatrix} 0 & 0 & 0 & 0 & 0 \\ 0 & 0 & 0 & -\frac{2}{3} & -\frac{2}{3}w \\ 0 & 0 & 0 & 0 & 0 \\ 0 & 1 & 0 & 0 & u \\ 0 & w & 0 & -\frac{2}{3}u & \frac{1}{3}uw \end{pmatrix}, \quad \tilde{\underline{B}}_{v,23}^{\mathcal{S}} = \begin{pmatrix} 0 & 0 & 0 & 0 & 0 \\ 0 & 0 & 0 & 0 & 0 \\ 0 & 0 & 0 & -\frac{2}{3} & -\frac{2}{3}w \\ 0 & 0 & 1 & 0 & v \\ 0 & 0 & w & -\frac{2}{3}v & \frac{1}{3}vw \end{pmatrix}, \end{aligned} \quad (132)$$

and can be decomposed as $\tilde{\mathcal{B}}_v^S = \mathcal{L}_v^{S,T} \mathcal{D}_v^S \mathcal{L}_v^S$ with,

$$\begin{aligned} \mathcal{D}_v^S &= \text{diag} \left(0, \frac{4}{3}, 1, 1, \frac{\theta p}{\rho}, 0, 0, 1, 1, \frac{\theta p}{\rho}, 0, 0, 0, 0, \frac{\theta p}{\rho} \right), \\ \underline{L}_{v,11}^S &= \begin{pmatrix} 0 & 0 & 0 & 0 & 0 \\ 0 & 1 & 0 & 0 & u \\ 0 & 0 & 1 & 0 & v \\ 0 & 0 & 0 & 1 & w \\ 0 & 0 & 0 & 0 & 1 \end{pmatrix}, \quad \underline{L}_{v,22}^S = \begin{pmatrix} 0 & 0 & 0 & 0 & 0 \\ 0 & 0 & 0 & 0 & 0 \\ 0 & 0 & 1 & 0 & v \\ 0 & 0 & 0 & 1 & w \\ 0 & 0 & 0 & 0 & 1 \end{pmatrix}, \quad \underline{L}_{v,33}^S = \begin{pmatrix} 0 & 0 & 0 & 0 & 0 \\ 0 & 0 & 0 & 0 & 0 \\ 0 & 0 & 0 & 0 & 0 \\ 0 & 0 & 0 & 0 & 0 \\ 0 & 0 & 0 & 0 & 1 \end{pmatrix}, \\ \underline{L}_{v,12}^S &= \begin{pmatrix} 0 & 0 & 0 & 0 & 0 \\ 0 & 0 & -\frac{1}{2} & 0 & \frac{v}{2} \\ 0 & 1 & 0 & 0 & u \\ 0 & 0 & 0 & 0 & 0 \\ 0 & 0 & 0 & 0 & 0 \end{pmatrix}, \quad \underline{L}_{v,13}^S = \begin{pmatrix} 0 & 0 & 0 & 0 & 0 \\ 0 & 0 & 0 & -\frac{1}{2} & \frac{w}{2} \\ 0 & 0 & 0 & 0 & 0 \\ 0 & 1 & 0 & 0 & u \\ 0 & 0 & 0 & 0 & 0 \end{pmatrix}, \quad \underline{L}_{v,23}^S = \begin{pmatrix} 0 & 0 & 0 & 0 & 0 \\ 0 & 0 & 0 & 0 & 0 \\ 0 & 0 & 0 & -1 & -w \\ 0 & 0 & 1 & 0 & v \\ 0 & 0 & 0 & 0 & 0 \end{pmatrix} \\ \underline{L}_{21}^S &= 0, \quad \underline{L}_{31}^S = 0, \quad \underline{L}_{32}^S = 0. \end{aligned} \tag{133}$$

D Guermond–Popov viscous flux with thermodynamic entropy variables

The artificial viscosity of Guermond and Popov [19] that we showed in (14) can be rewritten in matrix form when expressed in terms of the entropy variables,

$$\overset{\leftrightarrow}{\mathbf{f}}_{\text{GP}}^S = \mathcal{B}_{\text{GP}} \vec{\nabla} \mathbf{w}^S, \quad \mathcal{B}_{\text{GP}} = \alpha_a \rho \mathcal{B}_{\text{GP}}^\alpha + \mu_a p \mathcal{B}_{\text{GP}}^\mu, \tag{134}$$

where both block matrices, $\mathcal{B}_{\text{GP}}^\alpha$ and $\mathcal{B}_{\text{GP}}^\mu$ are,

$$\underline{B}_{\text{GP},ii}^\alpha = \frac{1}{\rho^2} \mathbf{q} \mathbf{q}^T + \Lambda^2 \mathbf{e}_5 \mathbf{e}_5^T = \begin{pmatrix} 1 & u & v & w & e \\ u & u^2 & uv & uw & ue \\ v & uv & v^2 & vw & ve \\ w & uw & vw & w^2 & ve \\ e & ue & ve & we & e^2 + \Lambda^2 \end{pmatrix}, \quad \underline{B}_{\text{GP},ij}^\alpha = 0 \quad (i \neq j), \quad \Lambda = \frac{p/\rho}{\sqrt{\gamma-1}}, \tag{135a}$$

$$\begin{aligned} \underline{B}_{\text{GP},11}^\mu &= \begin{pmatrix} 0 & 0 & 0 & 0 & 0 \\ 0 & 1 & 0 & 0 & u \\ 0 & 0 & \frac{1}{2} & 0 & \frac{v}{2} \\ 0 & 0 & 0 & \frac{1}{2} & \frac{w}{2} \\ 0 & u & \frac{v}{2} & \frac{w}{2} & \frac{1}{2} (u^2 + v_{\text{tot}}^2) \end{pmatrix}, \quad \underline{B}_{\text{GP},22}^\mu = \begin{pmatrix} 0 & 0 & 0 & 0 & 0 \\ 0 & \frac{1}{2} & 0 & 0 & \frac{u}{2} \\ 0 & 0 & 1 & 0 & v \\ 0 & 0 & 0 & \frac{1}{2} & \frac{w}{2} \\ 0 & \frac{u}{2} & v & \frac{w}{2} & \frac{1}{2} (u^2 + v_{\text{tot}}^2) \end{pmatrix}, \\ \underline{B}_{\text{GP},33}^\mu &= \begin{pmatrix} 0 & 0 & 0 & 0 & 0 \\ 0 & \frac{1}{2} & 0 & 0 & \frac{u}{2} \\ 0 & 0 & \frac{1}{2} & 0 & \frac{v}{2} \\ 0 & 0 & 0 & 1 & w \\ 0 & \frac{u}{2} & \frac{v}{2} & w & \frac{1}{2} (u^2 + v_{\text{tot}}^2) \end{pmatrix}, \quad \underline{B}_{\text{GP},12}^\mu = \begin{pmatrix} 0 & 0 & 0 & 0 & 0 \\ 0 & 0 & 0 & 0 & 0 \\ 0 & \frac{1}{2} & 0 & 0 & \frac{u}{2} \\ 0 & 0 & 0 & 0 & 0 \\ 0 & \frac{v}{2} & 0 & 0 & \frac{uv}{2} \end{pmatrix}, \\ \underline{B}_{\text{GP},13}^\mu &= \begin{pmatrix} 0 & 0 & 0 & 0 & 0 \\ 0 & 0 & 0 & 0 & 0 \\ 0 & 0 & 0 & 0 & 0 \\ 0 & \frac{1}{2} & 0 & 0 & \frac{u}{2} \\ 0 & \frac{w}{2} & 0 & 0 & \frac{uw}{2} \end{pmatrix}, \quad \underline{B}_{\text{GP},23}^\mu = \begin{pmatrix} 0 & 0 & 0 & 0 & 0 \\ 0 & 0 & 0 & 0 & 0 \\ 0 & 0 & 0 & 0 & 0 \\ 0 & 0 & \frac{1}{2} & 0 & \frac{v}{2} \\ 0 & 0 & \frac{w}{2} & 0 & \frac{vw}{2} \end{pmatrix}. \end{aligned} \tag{135b}$$

We want to highlight here that, in this case, the density gradient is easily computed as,

$$\vec{\nabla} \rho = \rho \vec{\nabla} w_1^S + \rho u \vec{\nabla} w_2^S + \rho v \vec{\nabla} w_3^S + \rho w \vec{\nabla} w_4^S + \rho e \vec{\nabla} w_5^S = \mathbf{q}^T \vec{\nabla} \mathbf{w}^S, \tag{136}$$

an expression that we have found useful when implementing some of the algorithms derived in this document as, for instance, the computation of the shock sensor in (127). A Cholesky decomposition can also be performed to rewrite $\mathcal{B}_{\text{GP}} = \mathcal{L}_{\text{GP}}^T \mathcal{D}_{\text{GP}} \mathcal{L}_{\text{GP}}$ where,

$$\begin{aligned} \mathcal{D}_{\text{GP}} &= \text{diag} \left(\alpha_a \rho, \mu_a p, \frac{1}{2} \mu_a p, \frac{1}{2} \mu_a p, \alpha_a \rho, \alpha_a \rho, 0, \mu_a p, \frac{1}{2} \mu_a p, \alpha_a \rho, \alpha_a \rho, 0, 0, \mu_a p, \alpha_a \rho \right), \\ \underline{L}_{11}^{\text{GP}} &= \begin{pmatrix} 1 & u & v & w & e \\ 0 & 1 & 0 & 0 & u \\ 0 & 0 & 1 & 0 & v \\ 0 & 0 & 0 & 1 & w \\ 0 & 0 & 0 & 0 & \Lambda \end{pmatrix}, \quad \underline{L}_{22}^{\text{GP}} = \begin{pmatrix} 1 & u & v & w & e \\ 0 & 0 & 0 & 0 & 0 \\ 0 & 0 & 1 & 0 & v \\ 0 & 0 & 0 & 1 & w \\ 0 & 0 & 0 & 0 & \Lambda \end{pmatrix}, \quad \underline{L}_{33}^{\text{GP}} = \begin{pmatrix} 1 & u & v & w & e \\ 0 & 0 & 0 & 0 & 0 \\ 0 & 0 & 0 & 0 & 0 \\ 0 & 0 & 0 & 1 & w \\ 0 & 0 & 0 & 0 & \Lambda \end{pmatrix}, \\ \underline{L}_{12}^{\text{GP}} &= \begin{pmatrix} 0 & 0 & 0 & 0 & 0 \\ 0 & 0 & 0 & 0 & 0 \\ 0 & 1 & 0 & 0 & u \\ 0 & 0 & 0 & 0 & 0 \\ 0 & 0 & 0 & 0 & 0 \end{pmatrix}, \quad \underline{L}_{13}^{\text{GP}} = \begin{pmatrix} 0 & 0 & 0 & 0 & 0 \\ 0 & 0 & 0 & 0 & 0 \\ 0 & 0 & 0 & 0 & 0 \\ 0 & 1 & 0 & 0 & u \\ 0 & 0 & 0 & 0 & 0 \end{pmatrix}, \quad \underline{L}_{23}^{\text{GP}} = \begin{pmatrix} 0 & 0 & 0 & 0 & 0 \\ 0 & 0 & 0 & 0 & 0 \\ 0 & 0 & 0 & 0 & 0 \\ 0 & 0 & 1 & 0 & v \\ 0 & 0 & 0 & 0 & 0 \end{pmatrix}, \\ \underline{L}_{21}^{\text{GP}} &= \underline{L}_{31}^{\text{GP}} = \underline{L}_{32}^{\text{GP}} = 0. \end{aligned} \tag{137}$$

References

1. W. H. Reed, T. R. Hill, Triangular mesh methods for the neutron transport equation, 1977, p. 23.
2. B. Cockburn, G. E. Karniadakis, C.-W. Shu, The development of discontinuous Galerkin methods (2000).
3. M. Woopen, A. Balan, G. May, J. Schütz, A comparison of hybridized and standard DG methods for target-based hp-adaptive simulation of compressible flow, *Computers & Fluids* 98 (2014) 3–16.
4. M. Kompenhans, G. Rubio, E. Ferrer, E. Valero, Adaptation strategies for high order discontinuous Galerkin methods based on tau-estimation, *Journal of Computational Physics* 306 (2016) 216–236.
5. L. Friedrich, A. R. Winters, D. C. D. R. Fernández, G. J. Gassner, M. Parsani, M. H. Carpenter, An entropy stable h / p non-conforming discontinuous Galerkin method with the summation-by-parts property, *Journal of Scientific Computing* 77 (2018) 689–725.
6. G. Ntoukas, J. Manzanero, G. Rubio, E. Valero, E. Ferrer, A free-energy stable p-adaptive nodal discontinuous Galerkin for the Cahn–Hilliard equation, *Journal of Computational Physics* 442 (2021) 110409.
7. E. F. Toro, *Riemann Solvers and Numerical Methods for Fluid Dynamics*, Springer Berlin Heidelberg, 2009.
8. A. Harten, On the symmetric form of systems of conservation laws with entropy, *Journal of Computational Physics* 49 (1983) 151–164.
9. E. Tadmor, A minimum entropy principle in the gas dynamics equations, *Applied Numerical Mathematics* 2 (1986) 211–219.
10. E. Tadmor, Entropy stability theory for difference approximations of nonlinear conservation laws and related time-dependent problems, *Acta Numerica* 12 (2003) 451–512.
11. D. A. Kopriva, *Implementing Spectral Methods for Partial Differential Equations*, Springer Netherlands, 2009.
12. B. Strand, Summation by parts for finite difference approximations for d/dx, *Journal of Computational Physics* 110 (1994) 47–67.
13. R. Abgrall, J. Nordström, P. Öffner, S. Tokareva, Analysis of the SBP-SAT stabilization for finite element methods part i: Linear problems, *Journal of Scientific Computing* 85 (2020).
14. A. Kravchenko, P. Moin, On the effect of numerical errors in large eddy simulations of turbulent flows, *Journal of Computational Physics* 131 (1997) 310–322.
15. S. Hennemann, A. M. Rueda-Ramírez, F. J. Hindenlang, G. J. Gassner, A provably entropy stable subcell shock capturing approach for high order split form dg for the compressible euler equations, *Journal of Computational Physics* 426 (2021) 109935.
16. P.-O. Persson, J. Peraire, Sub-cell shock capturing for discontinuous Galerkin methods, *Collection of Technical Papers - 44th AIAA Aerospace Sciences Meeting* 2 (2006) 1408–1420.
17. A. Klöckner, T. Warburton, J. S. Hesthaven, Viscous shock capturing in a time-explicit discontinuous Galerkin method, *Mathematical Modelling of Natural Phenomena* 6 (2011) 57–83.

18. D. Gottlieb, J. Hesthaven, Spectral methods for hyperbolic problems, *Journal of Computational and Applied Mathematics* 128 (2001) 83–131.
19. J. L. Guermond, B. Popov, Viscous regularization of the Euler equations and entropy principles, *SIAM Journal on Applied Mathematics* 74 (2014) 284–305.
20. G.-S. Karamanos, G. E. Karniadakis, A spectral vanishing viscosity method for large-eddy simulations, *Journal of Computational Physics* 163 (2000) 22–50.
21. R. M. Kirby, S. J. Sherwin, Stabilisation of spectral/hp element methods through spectral vanishing viscosity: Application to fluid mechanics modelling, *Computer Methods in Applied Mechanics and Engineering* 195 (2006) 3128–3144.
22. R. Moura, S. Sherwin, J. Peiró, Eigensolution analysis of spectral/hp continuous Galerkin approximations to advection–diffusion problems: Insights into spectral vanishing viscosity, *Journal of Computational Physics* 307 (2016) 401–422.
23. D. Lodares, J. Manzanero, E. Valero, An entropy–stable discontinuous Galerkin approximation of the Spalart–Allmaras turbulence model for the compressible Reynolds Averaged Navier–Stokes equations, Under review in *Journal of Computational Physics* (2021).
24. J. Manzanero, E. Ferrer, G. Rubio, E. Valero, Design of a Smagorinsky spectral vanishing viscosity turbulence model for discontinuous Galerkin methods, *Computers & Fluids* 200 (2020) 104440.
25. R. M. Kirby, G. E. Karniadakis, Coarse resolution turbulence simulations with spectral vanishing viscosity-large-eddy simulations (SVV-LES), *Journal of Fluids Engineering* 124 (2002) 886–891.
26. R. Pasquetti, E. Séverac, E. Serre, P. Bontoux, M. Schäfer, From stratified wakes to rotor-stator flows by an SVV-LES method, *Comput. Fluid Dyn* 22 (2008) 261–273.
27. G. J. Gassner, A. R. Winters, F. J. Hindenlang, D. A. Kopriva, The BR1 scheme is stable for the compressible Navier–Stokes equations, *Journal of Scientific Computing* 77 (2018) 154–200.
28. K. O. Friedrichs, P. D. Lax, Systems of conservation equations with a convex extension, *Proceedings of the National Academy of Sciences* 68 (1971) 1686–1688.
29. M. L. Merriam, An entropy-based approach to nonlinear stability (1989).
30. T. C. Fisher, M. H. Carpenter, High-order entropy stable finite difference schemes for nonlinear conservation laws: Finite domains, *Journal of Computational Physics* 252 (2013) 518–557.
31. A. Jameson, Formulation of kinetic energy preserving conservative schemes for gas dynamics and direct numerical simulation of one-dimensional viscous compressible flow in a shock tube using entropy and kinetic energy preserving schemes, *Journal of Scientific Computing* 34 (2008) 188–208.
32. G. J. Gassner, A kinetic energy preserving nodal discontinuous galerkin spectral element method, *International Journal for Numerical Methods in Fluids* 76 (2014) 28–50.
33. G. J. Gassner, A. R. Winters, D. A. Kopriva, Split form nodal discontinuous galerkin schemes with summation-by-parts property for the compressible euler equations, *Journal of Computational Physics* 327 (2016) 39–66.
34. D. A. Kopriva, Metric identities and the discontinuous spectral element method on curvilinear meshes, *Journal of Scientific Computing* 26 (2006) 301–327.
35. A. R. Winters, D. A. Kopriva, G. J. Gassner, F. Hindenlang, Construction of modern robust nodal discontinuous galerkin spectral element methods for the compressible navier–stokes equations (2021).
36. D. A. Kopriva, A polynomial spectral calculus for analysis of dg spectral element methods, arXiv preprint arXiv:1704.00709 (2017).
37. G. J. Gassner, A skew-symmetric discontinuous galerkin spectral element discretization and its relation to sbp-sat finite difference methods, *SIAM Journal on Scientific Computing* 35 (3) (2013) A1233–A1253.
38. M. H. Carpenter, J. Nordström, D. Gottlieb, A stable and conservative interface treatment of arbitrary spatial accuracy, *Journal of Computational Physics* 148 (1999) 341–365.
39. J. Nordström, T. Lundquist, Summation-by-parts in time, *Journal of Computational Physics* 251 (2013) 487–499.
40. D. C. D. R. Fernández, J. E. Hicken, D. W. Zingg, Review of summation-by-parts operators with simultaneous approximation terms for the numerical solution of partial differential equations, *Computers & Fluids* 95 (2014) 171–196.
41. S. Pirozzoli, Generalized conservative approximations of split convective derivative operators, *Journal of Computational Physics* 229 (2010) 7180–7190.
42. P. Chandrashekar, Kinetic energy preserving and entropy stable finite volume schemes for compressible Euler and Navier–Stokes equations, *Communications in Computational Physics* 14 (2013) 1252–1286.

43. F. Bassi and S. Rebay, A high-order accurate discontinuous finite element method for the numerical solution of the compressible Navier-Stokes equations, *Journal of Computational Physics* 131 (2) (1997) 267 – 279.
44. J.-R. Carlson, Inflow/outflow boundary conditions with application to FUN3D (2011).
45. G. Mengaldo, D. D. Grazia, F. Witherden, A. Farrington, P. Vincent, S. Sherwin, J. Peiro, A guide to the implementation of boundary conditions in compact high-order methods for compressible aerodynamics, American Institute of Aeronautics and Astronautics, 2014.
46. E. Tadmor, Convergence of spectral methods for nonlinear conservation laws, *SIAM Journal on Numerical Analysis* 26 (1989) 30–44.
47. Y. Maday, S. M. O. Kaber, E. Tadmor, Legendre pseudospectral viscosity method for nonlinear conservation laws, *SIAM Journal on Numerical Analysis* 30 (1993) 321–342.
48. S. M. O. Kaber, A legendre pseudospectral viscosity method, *Journal of Computational Physics* 128 (1996) 165–180.
49. J. Nordström, A. R. Winters, Stable filtering procedures for nodal discontinuous galerkin methods, *Journal of Scientific Computing* 87 (2021) 1–9.
50. T. Lundquist, J. Nordström, Stable and accurate filtering procedures, *Journal of Scientific Computing* 82 (2020) 16.
51. F. J. Hindenlang, G. J. Gassner, D. A. Kopriva, Stability of wall boundary condition procedures for discontinuous galerkin spectral element approximations of the compressible euler equations, *Spectral and High Order Methods for Partial Differential Equations* (2020) 3.
52. M. Chávez-Modena, E. Ferrer, G. Rubio, Improving the stability of multiple-relaxation lattice boltzmann methods with central moments, *Computers & Fluids* 172 (2018) 397–409.
53. P. Solán-Fustero, A. Navas-Montilla, E. Ferrer, J. Manzanero, P. García-Navarro, Application of approximate dispersion-diffusion analyses to under-resolved Burgers turbulence using high resolution WENO and UWC schemes, *Journal of Computational Physics* 435 (2021) 110246.
54. J. Kou, A. Hurtado-de Mendoza, S. Joshi, S. L. Clainche, E. Ferrer, Eigensolution analysis of immersed boundary method based on volume penalization: applications to high-order schemes, arXiv preprint arXiv:2107.10155 (2021).
55. S. B. Pope, Turbulent flows, *Measurement Science and Technology* 12 (2001) 2020–2021.
56. W. M. van Rees, A. Leonard, D. I. Pullin, P. Koumoutsakos, A comparison of vortex and pseudo-spectral methods for the simulation of periodic vortical flows at high reynolds numbers, *Journal of Computational Physics* 230 (2011) 2794–2805.
57. C.-W. Shu, S. Osher, Efficient implementation of essentially non-oscillatory shock-capturing schemes, ii, in: *Upwind and High-Resolution Schemes*, Springer, 1989, pp. 328–374.